The Bar–Halo Interaction–II. Secular evolution and the religion of N-body simulations

Martin D. Weinberg⋆ and Neal Katz⋆

Department of Astronomy, University of Massachusetts, Amherst, 01003, USA

28 August 2018

ABSTRACT

This paper explores resonance-driven secular evolution between a bar and dark-matter halo using N-body simulations. We make direct comparisons to our analytic theory (Weinberg & Katz 2005) to demonstrate the great difficulty that an N-body simulation has representing these dynamics for realistic astronomical interactions. In a dark-matter halo, the bar's angular momentum is coupled to the central density cusp (if present) by the Inner Lindblad Resonance. Owing to this angular momentum transfer and self-consistent re-equilibration, strong realistic bars *WILL* modify the cusp profile, lowering the central densities within about 30% of the bar radius in a few bar orbits. Past results to the contrary (Sellwood 2006; McMillan & Dehnen 2005) may be the result of weak bars or numerical artifacts. The magnitude depends on many factors and we illustrate the sensitivity of the response to the dark-matter profile, the bar shape and mass, and the galaxy's evolutionary history. For example, if the bar length is comparable to the size of a central dark-matter core, the bar may exchange angular momentum without changing its pattern speed significantly. We emphasise that this apparently simple example of secular evolution is remarkably subtle in detail and conclude that an N-body exploration of any astronomical scenario requires a deep investigation into the underlying dynamical mechanisms for that particular problem to set the necessary requirements for the simulation parameters and method (e.g. particle number and Poisson solver). Simply put, N-body simulations do not divinely reveal truth and hence their results are not infallible. They are unlikely to provide useful insight on their own, particularly for the study of even more complex secular processes such as the production of pseudo-bulges and disk heating.

Key words: stellar dynamics — dark matter — cosmology: observations, theory — galaxies: formation — Galaxy: kinematics and dynamics

1 INTRODUCTION

Current theoretical work in galaxy evolution attempts to relate the epoch of galaxy formation to the state of galaxies today. This requires understanding an approximately ten gigayear interval over which disk galaxies are in a slowly changing near equilibrium state. Although this equilibrium will be punctuated by minor mergers, the formation of bars, and the excitation of spiral structure, the disk's existence tells us that these perturbations must be relatively mild.

As in Nature itself, cosmological simulations often produce barred disks. This has led to a cacophony of predictions about the importance and implications of bars to the overall evolution of galaxies in the presence of cuspy dark matter haloes. To summarise, theory predicts that bars can transfer angular momentum to haloes through resonances and most groups agree that the bar does slow (Sellwood 1981; Weinberg 1985; Hernquist & Weinberg 1992; Debattista & Sellwood 2000; Sellwood 2003; Athanassoula 2003; Holley-Bockelmann et al. 2005) although Valenzuela & Klypin (2003, hereafter VK) find a more modest slow down. Debattista & Sellwood (2000) use this and the observational evidence that bars are not slow rotators to constrain the density of the present day dark-matter halo. Weinberg & Katz (2002, hereafter WK02) argue that the angular

⋆ E-mail: weinberg@astro.umass.edu (MDW); nsk@astro.umass.edu (NK)

momentum deposited in the halo will change the halo density profile. This latter work was criticised by Sellwood (2006) and McMillan & Dehnen (2005) who argue that the results of WK02 do not occur in there simulations.

The goal of this paper and the previous companion paper, Weinberg & Katz (2005, hereafter Paper I), is an exposition of the underlying dynamical principles that govern secular evolution and their application to N-body simulations. In many cases of interest, the secular evolution is mediated by resonances and the implicit time dependence of an evolving system affects the subsequent evolution. We use a numerical technique in Paper I for solving the perturbation theory that allows arbitrary time dependence to be included. In other words, the history of the system does matter and time-asymptotic results (e.g. Landau damping or the Lynden-Bell & Kalnajs 1972 theory, hereafter LBK) do not give accurate results (Weinberg 2004). Guided by the numerical requirements derived in Paper I, we perform a series of simulations to illustrate the special features of the bar-halo resonant interaction, its dependence on the properties of the halo and the bar, and the implication for N-body simulations to properly model this interaction. We hope that our results will help to clarify and reconcile some of the apparently disparate findings of other research groups (op. cit.). Most importantly, we show that the details of the torque depend on all aspects of the interaction, the halo profile, the bar shape, bar strength, bar pattern speed and history and cannot simply be predicted by an application of the Chandrasekhar dynamical friction or LBK formula. For example, dynamical theory predicts that a bar inside of a homogeneous core will not slow appreciably, which contradicts the naive dynamical friction analogy; we also demonstrate this using an N-body simulation below.

An N-body simulation adds two additional complications to the dynamics of secular evolution. First, an individual particle passing through a resonance receives a perturbation that depends sensitively on its initial position in phase-space. The correct secular evolution is the net average of many such trajectories. In Nature, a dark matter halo most likely has $N \to \infty$ from the perspective of any simulation and, therefore, has no difficulty averaging over all of phase-space. The simulation, however, must have a sufficient number of particles in the vicinity of the resonance to obtain the correct net torque. Paper I calls the resulting requirement on the number of particles the *coverage criterion*. Second, representation of the dark-matter and stellar components by an unnaturally small number of particles leads to fluctuations in the gravitational potential. For modern simulations, the magnitude of these fluctuations yields a very long relaxation time but the interaction region for a resonance has a very small phase-space volume. Paper I shows that the noise is sufficient to cause orbits to random walk through resonances. Of course, if some orbits walk out of the resonance, others walk in. However for some resonances, ILR in particular, orbits should *linger* near the resonance for many rotation periods. This increases the amplitude and changes the dependence of the torque on the phase-space distribution. The fluctuation noise prevents this lingering and in so doing changes both the amplitude of the net torque and the location of the orbits in phase space receiving the torque. Paper I shows that natural noise sources like satellites and subhaloes will not destroy the lingering orbits. The existence of multiple regimes underlines the necessity of understanding the dynamical mechanisms *before* fully trusting the results of a simulation constructed to investigate unknown dynamics. Paper I develops two criteria, a *small-scale noise* particle number criterion that treats the scale typical of gravitationally softened particles and a *large-scale noise* criterion that describes scales typical of basis expansions.

For simulations in this paper, we will use a basis expansion code (also known by the Hernquist & Ostriker 1992 moniker *self-consistent field (SCF) code*) to solve the Poisson equation. Our variant of this method is reviewed in §2 along with the details of our initial conditions and the bar perturbation. We choose the expansion technique for three reasons: 1) it is fast, scaling as $\mathcal{O}(N)$ with small overhead; 2) it restricts spatial sensitivity to the scales of interest; and 3) it facilitates direct comparison to perturbation theory. Paper I shows that the coverage criterion and the small-scale noise criterion dominates for the bar problem considered here. The expansion technique eliminates the small-scale noise and, therefore, in this paper we are only able to address the breakdown of the coverage criterion. We encourage groups with particle-particle and particle-mesh codes to test their codes as outlined in Paper I for the effects of small-scale noise. We investigate centring in §3 and concur with Sellwood (2006) and McMillan & Dehnen (2005) that a rotating quadrupole fixed to be centred on one position leads to an $m = 1$ artifact in the halo. This can be remedied by giving the bar a monopole component, i.e. a mass, which allows it to establish its own centre naturally by conserving linear momentum, removing the $m = 1$ artifact. In §4, we simulate a bar's slow down, angular momentum transfer, and the subsequent evolution of the dark matter halo using a large bar. We show that a strong Inner Lindblad Resonance (ILR) exists in a cuspy dark-matter halo (e.g. Navarro et al. 1997, hereafter NFW). The coupling at the ILR together with the self gravity of the affected orbits drives the evolution of the inner cusp profile. A large bar decreases the particle number requirements derived in Paper I and, because our inner dark-matter halo has a scale-free (power law) profile, the same results should obtain with little dependence on the bar size for an appropriately scaled bar mass. We use this to investigate and corroborate the predictions by decreasing and the size and mass of the bar in §5.1. Then, in §5.2 we investigate the dependence on bar shape and pattern speed, and in §5.3 investigate the dependence on the dark matter halo profile. We compare with other published findings in §6 and end with a discussion and summary in §7.

2 N-BODY METHOD AND MODELS

2.1 Potential solver

The disk and dark matter halo are evolved using a three-dimensional self-consistent field algorithm (Weinberg 1999). This potential solver uses an orthogonal function expansion to represent the density and potential field. Truncation of this expansion, then, limits the spatial resolution scale. These expansions are very efficient computationally but are not adaptive. In most N-body methods, either the gravitational softening, introduced to decrease two-body scattering, or the grid cell size determines the spatial resolution. In such codes, it is the number of such spatial resolution elements within the simulation volume that determines the effective number of degrees of freedom, typically a very large number. Expansion codes limit the degrees of freedom, causing a large decrease in the small-scale noise, i.e. two-body relaxation, making this class of code ideal for simulating the long term evolution caused by resonant dynamics (Earn & Sellwood 1995; Clutton-Brock 1972, 1973; Kalnajs 1976; Polyachenko & Shukhman 1981; Fridman & Polyachenko 1984; Hernquist & Ostriker 1992; Hernquist et al. 1995; Brown & Papaloizou 1998; Earn 1996). As demonstrated in Paper I, the relaxation times for this code, when used with a radial and angular basis truncation sufficient for resolving all the important resonances, are orders of magnitude longer than a softened direct summation or tree code. Conversely, if one were to include enough radial and angular basis functions so that the same spatial resolution as a softened particle code were approached, the noise level and relaxation times would be comparable. The choice of a particular truncation introduces a bias by limiting the density and potential profiles to those that can be represented by such a basis. Nonetheless, for near-equilibrium secular evolution, the overall changes are likely to be on large spatial scales and to be gradual and, therefore, less affected by incompleteness.

Our potential solver exploits properties of the Sturm-Liouville (SL) equation to generate a numerical bi-orthogonal basis set whose lowest order basis function matches the equilibrium model. Many important physical systems in quantum and classical dynamics reduce to the SL form,

$$\frac{d}{dx}\left[p(x)\frac{d\Phi(x)}{dx}\right] - q(x)\Phi(x) = \lambda\omega(x)\Phi(x), \tag{1}$$

where λ is a constant and $\omega(x)$ is a known function called either the density or weighting function. If $\Phi(x)$ and $\omega(x)$ are positive in an interval $a < x < b$ then the SL equation is satisfied only for a discrete set of eigenvalues λ_j with corresponding eigenfunctions $\phi_j(x)$ where $j = 0, 1, \ldots$. The eigenfunctions form a complete basis set (Courant & Hilbert 1953) and can be chosen to be orthogonal with the following additional properties: 1) the eigenvalues λ_n are countably infinite and can be ordered: $\lambda_n < \lambda_{n+1}$; 2) there is a smallest non-negative eigenvalue, $\lambda_1 > 0$, but there is no greatest eigenvalue; and 3) the eigenfunctions, ϕ_n, possess nodes between a and b, and the number of nodes increases with increasing n, e.g. the eigenfunction $\phi_1(x)$ has no nodes, $\phi_2(x)$ has one node, etc.

In the special case of Poisson's equation, we use the eigenfunctions to construct biorthogonal density and potential pairs, d_k^{lm} and u_j^{lm} given by:

$$-\frac{1}{4\pi G}\int dr r^2 d_k^{lm\,*}(r)u_j^{lm}(r) = \delta_{jk}. \tag{2}$$

The lowest order potential-density pair ($j = k = 1$, $l = m = 0$) is defined to be the equilibrium profile, and the higher order terms represent deviations about this profile. This approach minimises the number of radial terms that one requires to reproduce both the unperturbed equilibrium and large-scale variations from this equilibrium. Weinberg (1999) shows that by assuming a gravitational potential of the form $\Phi(r) = \Phi_0(r)f(r)$ with physical boundary conditions for Poisson's equation and Φ_0 chosen to be the equilibrium field, the equation for $f(r)$ also takes the SL form and can be solved numerically to high accuracy using the Pruess & Fulton algorithm (Marletta & Pryce 1991; Pruess & Fulton 1993; Pryce 1993). Weinberg (1999) suggested the possibility of reconstructing the basis as the system evolves. Although this procedure has some advantages for studying long-term evolution, one must exercise great care to ensure that transient features are not frozen into the basis. For the simulations here, we fix the basis for the entire simulation.

We use a NFW profile truncated at large radii for our equilibrium halo model and as the zero-order radial basis function. We obtain a self-consistent phase-space distribution function for this model as follows. We use an Eddington inversion (e.g. Binney & Tremaine 1987) to derive the phase-space distribution function for the truncated profile, $\rho_0(r)$ and $\phi_0(r)$, and integrate this distribution over velocities to get $\rho_1(r)$ and $\phi_1(r)$. We then repeat the inversion to get a new distribution function and integrate to get $\rho_2(r)$ and $\phi_2(r)$ and so on. In practice, this procedure converges in several iterations. In many cases, we add an additional spherical component to the gravitational potential that represents the enclosed disk mass. The initial conditions are generated from random variates $\mathcal{R}$ by inverting the mass profile $\mathcal{R} = M(r)$ to get a spatial position and by using the acceptance-rejection method along with the phase-space distribution function to get a velocity. Models constructed this way are usually in good virial equilibrium to start, with $|2T/W + 1| \lesssim 0.01$ typically for $N = 10^6$ particles.

To improve the effective particle number in the dynamically important central density cusp, we generate initial conditions whose spatial number density is $n(r) \propto r^{-2.5}$, steeper than the spatial mass density of the inner NFW profile. We do this by determining the phase-space distribution function for this new number density profile by Eddington inversion as described
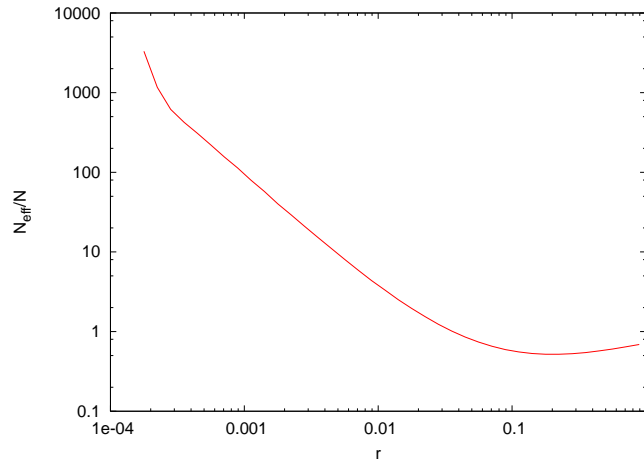
Figure 1. The ratio of the effective number of equal mass particles to the actual number of particles as a function of halo radius for our multimass equilibrium. The ratio is near unity for $r \gtrsim 0.01$ but increases to almost 1000 for the most bound particles in the simulation.

above. The assigned mass is then the mean mass per particle multiplied by the ratio of the *mass* phase-space distribution function to the *number* phase-space distribution function. At any given radius, we can then define the effective particle number, $N_{eff}(r) = M/\langle m \rangle_r$ where $\langle m \rangle_r$ is the mean particle mass at radius r. The ratio of N_{eff} to the total particle number N is shown in Figure 1. The values of N_{eff} in the cusp everywhere exceeds N. For example, an $N = 10^6$ multimass particle phase space is equivalent to a $N_{eff} = 10^8$ equal mass particle phase space for $r \leqslant 0.001$.

We retain halo basis terms up to $n_{\max} = 20$ and $l_{\max} = 4$. Particles are advanced using a leapfrog integrator, with a time step $1/50$ of the smallest orbital oscillation period. Such a small time step is required owing to the small interaction region around each resonance. This requirement varies with the bar model, as described later. We compared orbits integrated in the exact potential and using the perturbation approach from Paper I with the results of the N-body simulation to confirm our choice of time step and verify the insignificance of noise.

2.2   Details of the bar perturbation

We choose the bar to be a homogeneous ellipsoid with axes a_1, a_2, a_3 and ratios $a_1 : a_2 : a_3 :: 10 : y : 1$ with $2 \leqslant y \leqslant 7$. As described in §4, we choose our bar perturbation to be the monopole and quadrupole parts of this potential. The assumption of a homogeneous ellipsoid does not limit the applicability of our work to realistic bars owing to the weak dependence of the monopole and quadrupole components to the details of the ellipsoid. Rather, the ellipsoid sets the overall scale. The initial conditions are then constructed by adding the monopole to the NFW profile and performing the iterative Eddington inversion procedure. This allows the NFW density profile to be approximately maintained as the quadrupole part of the perturbation is slowly turned on over several bar rotation times.

The quadrupole is assumed to have the functional form:

$$\Phi_1(r, \theta, \phi) = Y_{22}(\theta, \phi) U_{22}(r) \tag{3}$$

where

$$U_{22}(r) = \frac{b_1 r^2}{1 + (r/b_5)^5} \tag{4}$$

This form has the correct solution to Laplace's equation at very small and very large values of r and is a good fit to the exact quadrupole (see §2.3). The derivation of b_1 and b_5 follows from the exact potential in terms of elliptic integrals (see Weinberg 1985). U_{22} peaks at $r = (2/3)^{1/5} b_5$ with the value $(2^2 3^3)^{1/5} b_1 b_5^2 / 5$. For this potential, the projected surface density along the minor axis is

$$\Sigma(x, y) = \frac{3M_b}{2\pi ab} \sqrt{1 - x^2/a^2 - y^2/b^2} \tag{5}$$

where M_b is the total bar mass. This form approximately describes the observed surface brightness of bars (Kormendy 1982). However, alternative profiles can be fit with equation (4) or the more general form below (eq. 7).

2.3   Comparison with bar quadrupole from Hernquist & Weinberg

We used the quadrupole form of equation (4) in WK, but a different form,
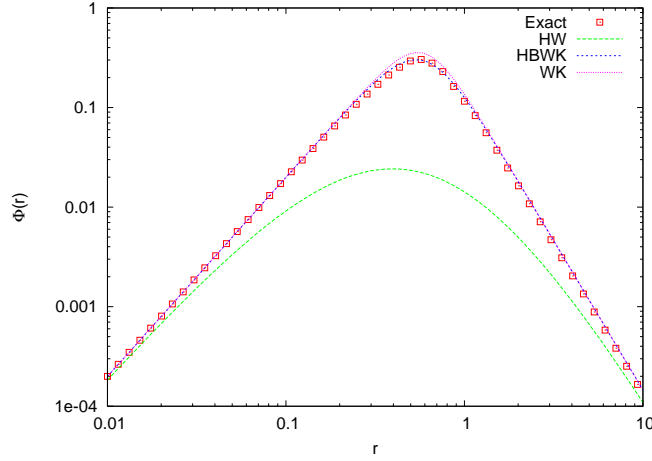
Figure 2. Comparison of the quadrupole potential fitting formula from HBWK, WK, and HW with the exact quadrupole potential of the homogeneous ellipsoid whose projected surface density is given in eq. 5. Notice that the HBWK bar, from a fully consistent disk + halo N-body simulation is indistinguishable from the exact homogeneous ellipsoid at quadrupole order.
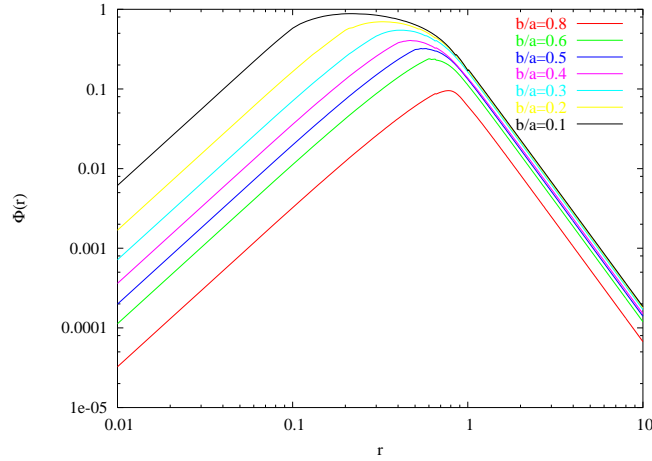
Figure 3. Comparison of the WK quadrupole potential fitting formula for bars with various axis ratios b/a with fixed $c/a = 1/20$. A smaller b/a yields a deeper quadrupole potential inside the bar radius, which increases the torque for small energy cusp orbits.

$$U_{22}(r) = \frac{b_1 r^2}{[1 + r/b_5]^5}, \tag{6}$$

in Hernquist & Weinberg (1992, hereafter HW). Both of these can be included in the more general form

$$U_{22}(r) = \frac{b_1 r^2}{[1 + (r/b_5)^\alpha]^{5/\alpha}} \tag{7}$$

while still maintaining the same asymptotic radial dependence consistent with the Laplace equation. Equation (6) results for $\alpha = 1$ and equation (4) results for $\alpha = 5$. Figure 2 compares these two fitting formula to the exact potential of a homogeneous ellipsoid. In both cases b_1 and b_5 are chosen to match the exact potential at small and large r. Holley-Bockelmann et al. (2005, hereafter HBWK) find stellar bars, formed self-consistently in N-body simulations, have $\alpha \approx 4$. As shown in the figure, the quadrupole from the ellipsoid is a very good match to the quadrupole derived from the N-body bar. Equation (4) nearly matches the exact potential for the ellipsoid while equation (6) underestimates the peak of the potential by more than an order of magnitude. This difference would have a significant effect on the total torque.

Different bar profiles may require tuning the value of α. Increasing values of α in equation (7) increases the sharpness of the turn over between the r^2 and r^{-3} tails; the profile becomes a discontinuous broken power law as $\alpha \to \infty$. Kormendy (1982) reports that along the major axis the surface brightness is nearly constant interior to a sharp outer edge, while along the minor axis the profile is steep, as in an $r^{1/4}$ law. The approximation $\Sigma(x, y)$ above is, therefore, a good representation of the major axis although it falls off more gradually along the projected minor axis. One can compensate for this by decreasing the ratio of a_2/a_1. Moreover, our fiducial choice of $a_2/a_1 = 1/5$ (see §2.2) is similar to those of many bars (Kormendy 1982). Figure

3 shows that a smaller a_2/a_1 gives a larger amplitude quadrupole inside the bar radius, which will increase the efficiency of coupling to lower energy orbits.

3   DIPOLE RESPONSE AND THE EXPANSION CENTRE

Application of equation (3) as a bar perturbation requires a prior knowledge of the galaxy's centre. Although our simulations contain sufficient particles such that the root mean square drift of the centre will be negligible, inclusion of the $l = 1$ term in the potential solver with a fixed-centre quadrupole promotes an instability between the bar and halo, which changes the angular momentum exchange by amplifying the offset of their two centres. A small shift between the quadrupole and halo centre, which could be generated by particle noise, converts some of the bar's angular momentum into linear momentum of the halo cusp. This increases the $l = 1$ amplitude and leads to a run away. The consequences of this were noted by Sellwood (2003). This instability may be removed by adding the monopole term to equation (3):

$$\Phi_1(\bar{r}, \bar{\theta}, \bar{\phi}) = Y_{00}(\bar{\theta}, \bar{\phi})U_{00}(\bar{r}) + Y_{22}(\bar{\theta}, \bar{\phi})U_{22}(\bar{r}) \tag{8}$$

where $\bar{\mathbf{r}}$ is the coordinate the bar frame and U_{00} is the monopole part of the bar potential. We compute the origin of the bar frame by conserving linear momentum in the combined bar–halo mass distribution. The restoring force resulting from the addition of inertial and gravitational mass causes the bar to oscillate weakly about the centre and damps the $m = 1$ instability. We have performed simulations both without the $l = 1$ term and using only the even l terms and, when one includes the monopole part of the bar potential, we obtained nearly identical torque curves $L_z = L_z(t)$ as when all the terms are included. In most cases, we choose the monopole and quadrupole to be consistent with a single homogeneous ellipsoid, however, this is not a requirement. As long as the $m = 1$ instability does not grow, the quadrupole amplitude can be adjusted independently of the monopole to mimic a bar that lengthens and changes shape.

By adding the monopole component to the bar potential we successfully damped the $m = 1$ instability. However, since the bar centre and central density cusp can now be offset, the central density cusp is no longer necessarily centred on the Poisson expansion, which could introduce another problem. If the offset from the expansion centre became large enough then our finite number of expansion terms would cause the gravitational forces within the cusp to be underestimated and the cusp could artificially dissolve. We check the position of the cusp relative to the expansion origin by computing the centre of mass of the most bound particles such that we include a mass fraction of $5 \times 10^{-4} M_{vir}$. For example, for 10^6 equal mass particles within the virial radius, we compute the centre for the 500 most bound particles. Even if the bar is free to move relative to the density cusp, the typical offset of the density cusp from the expansion centre is only several hundredths of a percent of the virial radius. For the number of terms we keep in our Poisson expansion, i.e. $n_{max} = 20$ and $l_{max} = 4$, the central cusps of equilibrium NFW halos evolved with offsets from the expansion centre of this size remain in equilibrium for over 5 Gyrs, mitigating any need for concern.

We choose the pattern speed of the bar, Ω_p, to be the circular frequency in the unperturbed halo at some multiple of the bar length, a_1. The angular momentum of the bar is then:

$$L_{z,bar} = \Omega I_z, \tag{9}$$

$$I_z = \frac{1}{5}(a_1^2 + a_2^2)M_b. \tag{10}$$

The pattern speed at any future time is determined directly from momentum conservation for the combined bar–halo system as follows. Initially, we compute the total angular momentum content of the halo ($L_{z,halo}$), add this to the bar angular momentum, ($L_{z,bar}$), and keep this constant. The pattern speed is then

$$\Omega_p = (L_{z,bar} + L_{z,halo} - L_{z,t})/I_z \tag{11}$$

where $L_{z,t}$ is the angular momentum of the halo at time t. This model, of course, neglects angular momentum transport between the bar and the rest of the disk; this is explicitly investigated and quantified in HBWK.

4   FIDUCIAL RUN

Our fiducial run uses an NFW halo with a concentration parameter of $c = 15$. Our fiducial bar has a length equal to the NFW scale length r_s, a mass equal to $1/2$ the mass of the halo enclosed within that radius, and a shape $a_1 : a_2 : a_3 :: 10 : 2 : 1$. The perturbation is turned on over approximately a bar rotation time. The bar pattern speed is adjusted during the simulation to conserve the total angular momentum of the bar–halo system (eq. 11). This bar radius is unrealistically large compared to present-day bars, but this choice ensures that all of the particle number criteria obtained in Paper I are satisfied. However, because the NFW profile is scale free inside of r_s, one should not expect significant differences for smaller bars scaled to the same enclosed dark-matter mass. We will discuss smaller present-day-sized bars in §5.1.
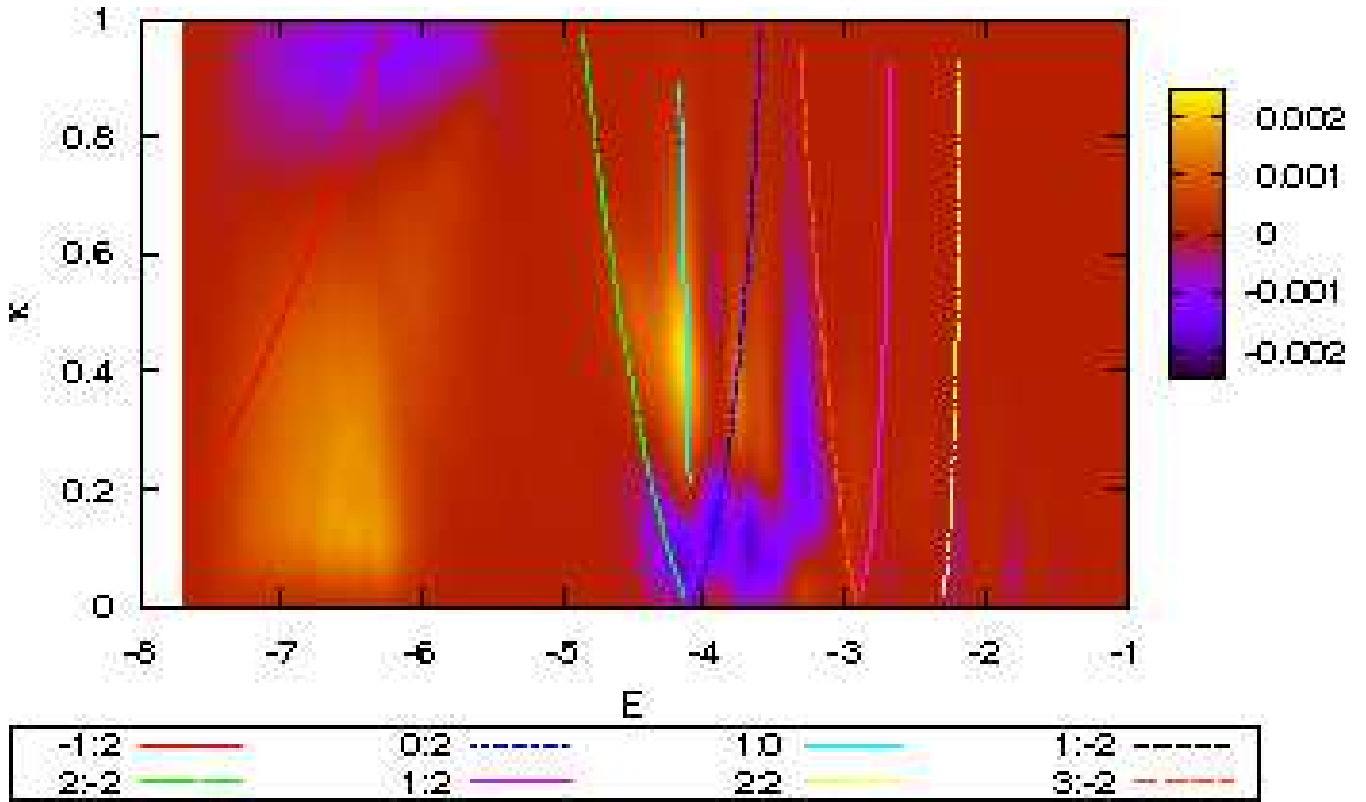
Figure 4. Distribution of ΔL_z for the slowing fiducial bar with the locations of low-order resonances $l_1 : l_2$ at the pattern speed of peak torque overlayed.

The bar perturbation is turned on over several bar rotation times using an error function as follows:

$$A(t) = \frac{A_o}{2} \left\{ 1 + \mathrm{erf}[(t - t_0)/\delta] \right\} \tag{12}$$

where $A(\infty) = A_o$ is the final quadrupole amplitude. The amplitude of the monopole term, now integral to the overall equilibrium, is not adjusted. For the simulations described below, we set $t_0 = 1/2$ and $\delta = 1/4$ unless otherwise stated. In Paper I we used a slower turn on to investigate the detailed dynamical mechanism. Here, our turn on rate is motivated by bar formation times observed in self-consistent simulations (HBWK). Scaled to the Milky Way, one time unit is approximately 2 Gyr. Variations in t_0 and δ or the choice $A(t) = $ constant do not make large differences in the results since the strongest coupling is driven by the slowing of the bar (Weinberg 2004). To compare models with different parameters t_0 and δ, we define a scaled time $\tau \equiv \int_0^t dt\, A(t)$. This is the equivalent time for a full-strength bar. In an N-body simulation without the bar perturbation, the dark matter halo profile is indistinguishable from the initial profile after 3 time units (approx. 6 Gyr for the Milky Way).

We use 10^6 multimass particles for investigating the large bars with fiducial parameters but smaller bars require larger N as we will see in later sections. The criteria calculations from Paper I predict that $N \approx 10^8$ equal mass particles within the virial radius are needed for ILR and $N \lesssim 10^6$ equal mass particles for the other low-order resonances. The effective particle number in the vicinity of ILR (see Paper I) for $N = 10^6$ is between 10^7 and 10^8 equal mass particles within the virial radius and this provides sufficient coverage for all but possibly the most eccentric orbits near the ILR for our large fiducial bar. However, this particle number is not sufficient for a scale-length sized bar, which requires $N \gtrsim 10^9$ equal mass particles.

4.1 Description and theoretical interpretation

The resonant angular exchange mechanism deposits (or extracts) angular momentum in (from) the dark matter halo at specific regions in phase space. Hence, as we discuss in Paper I, plotting the change in angular momentum over a finite time is a good way to see the important resonances. In Figure 4, we show the ensemble change in the z component of the angular momentum ΔL_z in phase-space during the evolution of the fiducial bar. An equilibrium phase-space distribution in a spherical halo is described by two conserved quantities and for a clearer presentation we use the energy E and the angular momentum scaled to the maximum for a given energy $\kappa \equiv J/J_{max}(E) \in [0, 1]$. This figure is made by first computing ΔL_z for each orbit as a function of its initial values of E and κ. We then use kernel density estimation with cross validation (Silverman 1986) to
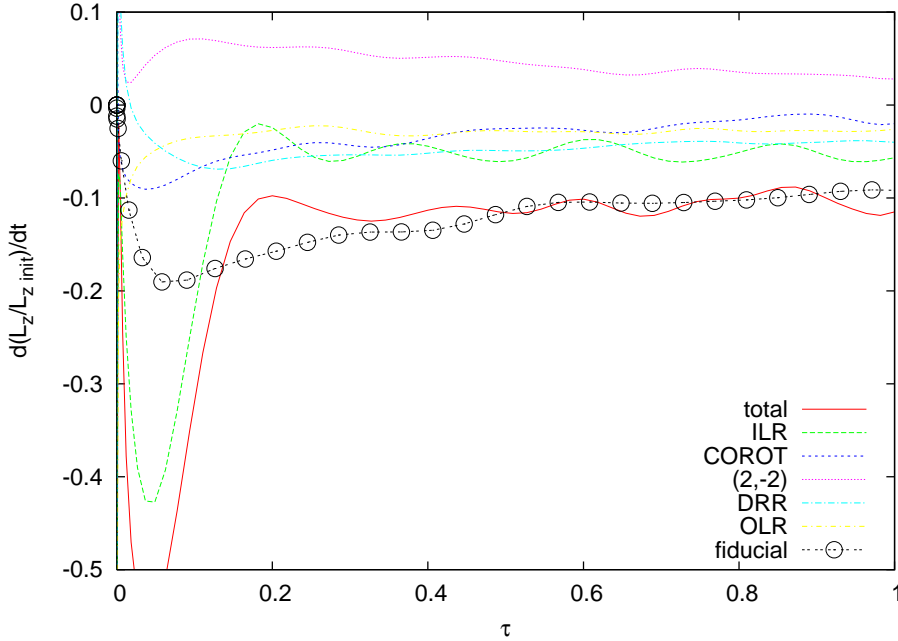
Figure 5. The torque $\Delta L_z / \Delta t$ versus scaled time τ from the fiducial model compared with the perturbation theory predictions from Paper I for the total torque and for the torque from individual resonances.

estimate the smoothing kernel. We increase and decrease this estimate to ensure that the resulting density field is not over smoothed. In the figure, we also indicate the positions of the low-order resonances, calculated at the bar pattern speed when the torque is largest. However, since the bar pattern speed changes with time so will the position of the resonances in phase space. This makes the ILR less obvious because it is spread over a large range in energy owing to the time-dependence of the frequency spectrum of the slowing bar. This resonance, $(-1, 2, 2)$ [1], has a particularly interesting degeneracy. As $\Omega_p \to 0$, there is always some value $\kappa \to 0$ such that $l_1 \Omega_r + l_2 \Omega_\phi \to m \Omega_p$. The limiting case is a purely radial orbit. In a cuspy profile, the orbital frequencies Ω_j increase as the energy decreases so that there is also some bit of phase space near resonance. This resonance track continues to smaller values of E and κ. Unlike the non-degenerate low-order resonances, for ILR a small change in Ω_p can have a large effect on the relative location of the resonance track.

In an evolving system, the frequency spectrum is broadened, and this promotes coupling to the ILR over a large range of radii. Paper I describes the application of canonical perturbation theory to time-dependent secular evolution using a numerical procedure. The perturbation theory allows investigation of each resonance separately. We compare the perturbation theory predictions to our fiducial bar simulation in Figure 5. The perturbation theory predicts that the ILR is responsible for approximately half of the total torque during the rapid phase of bar slowing. However, since the strength of the bar perturbation causes the interaction to be nonlinear, the linear perturbation theory is scaled beyond its domain of validity, which results in the mismatch at early times ($\tau \lesssim 0.2$). Because we do not expect the perturbation theory to match the stronger bar simulation precisely as it did for the weak bars considered in Paper I, the exact comparison is less useful here than are the relative contributions of each resonance. After the initial nonlinear phase, the ILR, the direct radial resonance $(1, 0, 2)$ [hereafter, DRR], and the $(2, -2, 2)$ resonances account for approximately 25% of the total torque each and corotation and OLR are 15% and 10% of the total, respectively. Also note that the $(2, -2, 2)$ resonance *supplies* angular momentum to the bar. After the bar slows substantially, the ILR becomes a less efficient angular momentum sink, requiring increasingly high-eccentricity orbits for coupling to the cusp and the remaining low-order resonances move to large radii where the coupling is also weak. As we show in Paper I, the ILR is the most numerically difficult resonance to reproduce in N-body simulations. If numerical deficiencies cause the ILR to be missed or weakened, the net torque on the bar can be greatly reduced. Since, of the remaining resonances, DRR and $(2, -2, 2)$ have comparable strengths but opposite signs and effect similar radii, in this numerically compromised case only the net effect of corotation and OLR will slow the bar and the angular momentum will be deposited at larger radii in the halo, at about the bar radius.

We plot the bar pattern speed evolution in Figure 6. The initial bar period is 0.3 time units and the bar reaches half of its full amplitude at $t = 0.5$ ($\tau = 0.07$). At about this time the bar begins to slow rapidly. As described above, the

---

[1] The resonance condition may be written $l_1 \Omega_r + l_2 \Omega_\phi = m \Omega_p$ for a spherical model. We denote a particular resonance by the triple (l_1, l_2, m). When we are considering $m = 2$ specifically, we shorten the designation to (l_1, l_2).
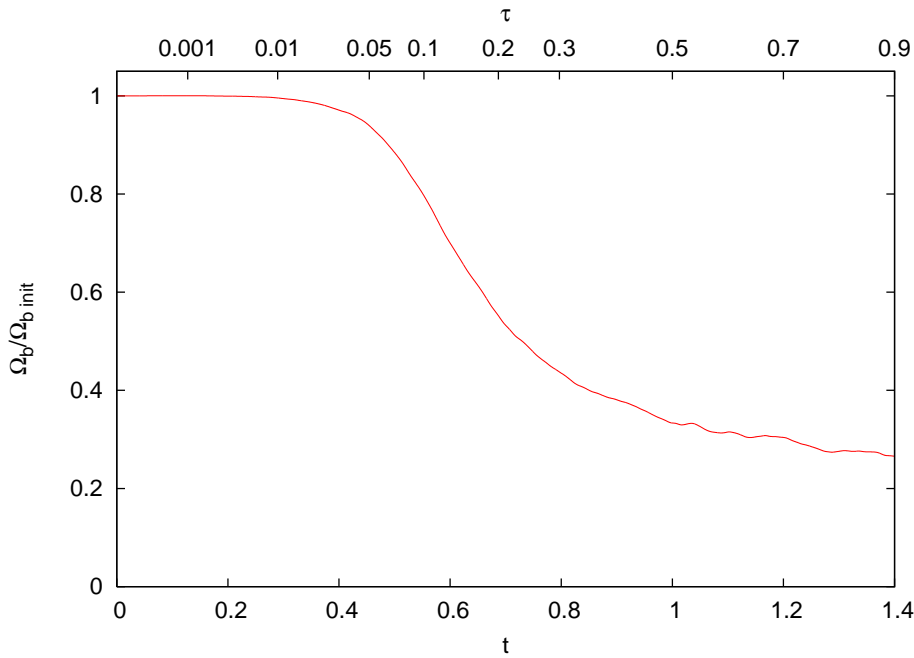
Figure 6. Evolution of the fiducial bar's pattern speed in physical time t (lower axis) and scaled time τ (upper axis).


(a) Evolving pattern speed

(b) Fixed pattern speed
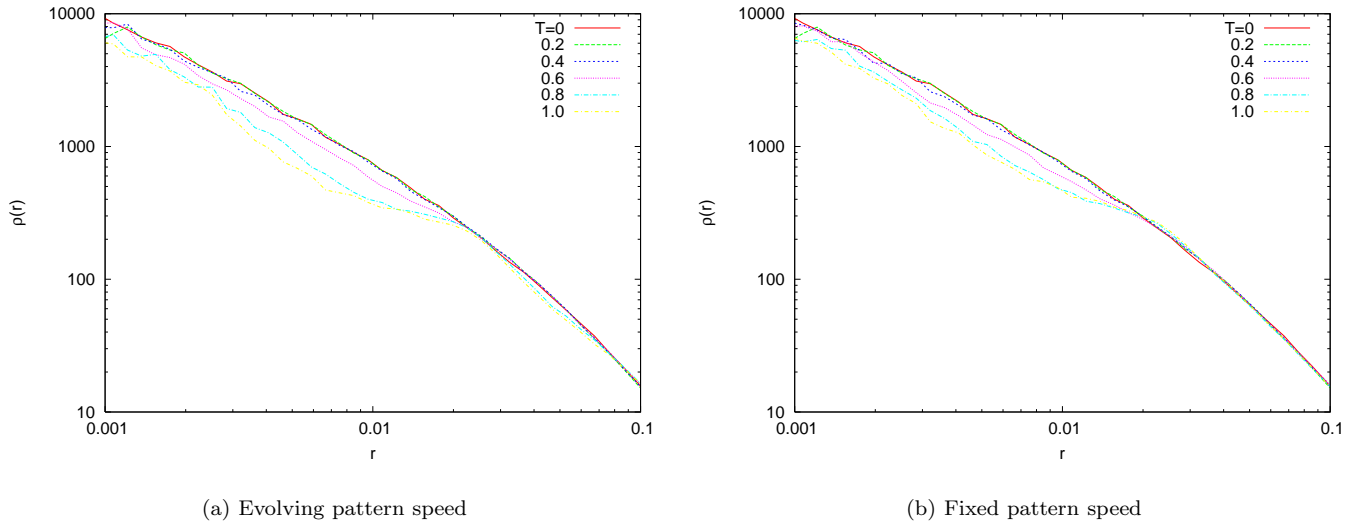
Figure 7. Evolution of the halo density profile shown as function of time T. The initial bar period is 0.3 time units.

angular momentum loss is dominated by the ILR $(-1, 2, 2)$ and DRR. As we discussed in WK02, the addition of this angular momentum causes the halo density profile to evolve. We show the bar-driven evolution of the dark matter density profile for the fiducial model in Figure 7a. The orbits affected by the ILR have characteristic radii well inside the bar radius. The corotation radius begins at the end of the bar and slowly moves outward as the bar slows, while the ILR moves inwards. The DRR occurs close to but inside of corotation. The initial bar radius is $r_s = 0.067$ and the peak of the profile evolution occurs at a radius of 0.01, a factor of six smaller in radius. Note that this profile evolution occurs even though we added a monopole component to the bar potential and hence removed the $m = 1$ instability.

Even if the bar does not slow at all the halo density profile still evolves. We plot the evolution of the profile for this fixed-pattern-speed case in Figure 7b and it shows the same overall trend as for the evolving bar. However, the evolution in the fixed-pattern case is driven only by the evolving halo and the creation of the bar and not by the pattern speed evolution and, therefore, is weaker. For times longer than $t \gtrsim 1$, the evolution of the inner profile ceases for our fiducial bar, since the bar has mostly stopped slowing at this time. We restarted a fresh bar in the evolved phase space at $t = 1$ and the evolution
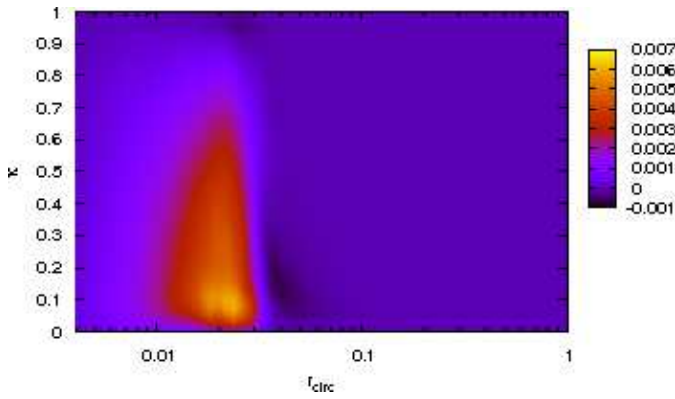
Figure 8. The distribution of z-angular momentum change (ΔL_z) in the halo phase space plotted as a function of r_{circ} and $\kappa = J/J_{max}$ predicted by perturbation theory. The quantity r_{circ} is the radius of a circular orbit with the same energy.
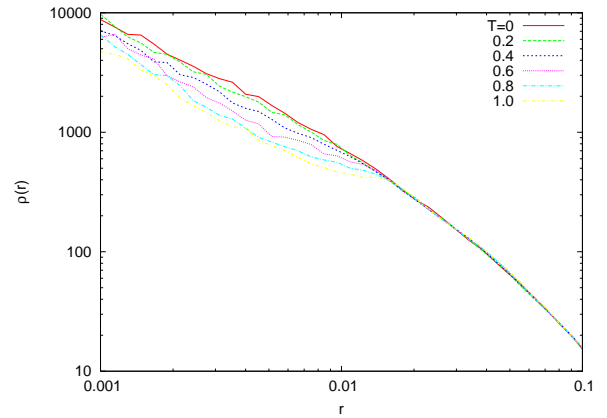
Figure 9. The evolution of the halo profile shown as a function of time T after adding the distribution of ΔL_z shown in Figure 8 over one time unit.

continued for another time unit. This indicates that the finite life time of the bar is spreading power to lower frequencies, where it can be resonantly absorbed by the halo cusp; we have predicted this transient analytically using the methods of Paper I.

4.2 Profile evolution explained

Figure 8 shows the phase-space distribution of angular momentum change ΔL_z during one time unit (in units with $M_{vir} = R_{vir} = 1$) for the ILR as the bar slows. This distribution was computed using the perturbation theory approach used in Paper I and plotted as in Figure 4. Rather than plotting energy E and scaled angular momentum $\kappa \equiv J/J_{max}$, however, we plot the radius of the circular orbit with the same energy E, called r_{circ}. For $\kappa \sim 1$, the radius of the actual orbit will be well approximated by r_{circ}, but for $\kappa \sim 0$, the pericentric radius will be much smaller than r_{circ}, making the apocentric radius $\mathcal{O}(r_{circ})$. Since the largest values of ΔL_z occur at small values of κ, the torqued radial orbits have an effect on the cusp well inside r_{circ}. Of course, to follow the effect on the new equilibrium profile one must allow the phase space to self consistently readjust to the new equilibrium. Comparing Figures 7 and 8 shows that the radii that have the greatest profile evolution are the same radii with the greatest angular momentum change, suggesting that the profile evolution owes to angular momentum transfer at ILR.

As further evidence, we perform a simulation in which we add the perturbation theory predicted change in angular momentum (from Figure 8) at each point in phase space to an equilibrium NFW halo, continuously over one time unit and allow the system to reach a new equilibrium. More precisely, at each time step we use Figure 8 to estimate the time-averaged torque $T_z = \Delta L_z/\Delta t$, then we compute the values of E and κ for each particle, then we compute T_z by interpolation, and finally we accelerate the particle in azimuth to reproduce $\Delta L_z = T_z \Delta t$. The resulting density profiles are shown in Figure 9 and are a very close match to those in Figure 7a, demonstrating that the deposition of angular momentum at ILR and subsequent re-equilibration drives the profile evolution. In principle, any torque received by the halo must change the underlying equilibrium profile. The change in the cusp appears dramatic because of the low overall specific angular momentum of the ILR-coupled cusp orbits relative to the bar angular momentum and the crucial role these orbits play in sustaining the self gravity of the cusp. The response would presumably be smaller for a steeper cusp, which would have a larger fractional binding energy.

5 DEPENDENCE ON MODEL PARAMETERS

5.1 Variation of bar size and bar mass

In the past section we discussed the results for our fiducial bar, which is much larger than bars found in galaxies today. Here, we discuss the evolution of both shorter bars and those with different masses. The different bar lengths and masses that we investigate are presented in Table 1. Since the inner parts of a NFW profile are a power law, it is scale free inside of r_s, which is the length of our largest bar. Therefore, the evolution of shorter bars should scale as the bar remains the same fraction of the enclosed mass, and the corotation radius remains the same number of bar lengths. Perturbation theory predicts a well-defined scaling of the overall angular momentum evolution with bar mass, more precisely with the perturbation strength. However, the scaling depends on the nature of the resonant interaction. If the evolution is fast enough, an orbit passes through

(a) Fast-limit scaling

(b) 50% fast-limit + 50% slow-limit scaling
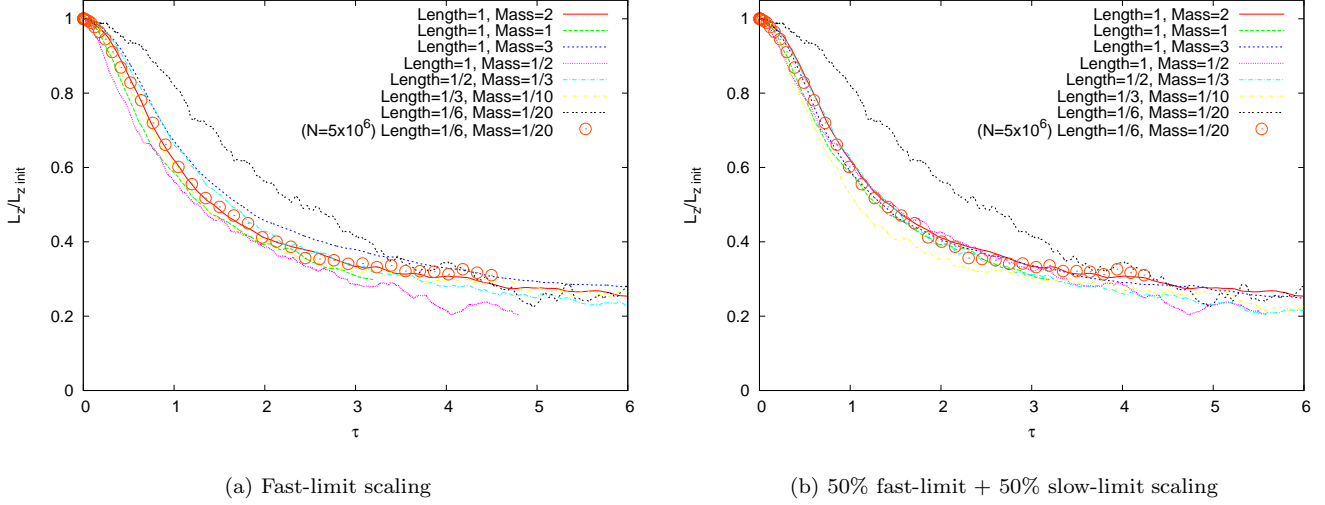
Figure 10. The change in L_z for slowing bars of different masses and sizes scaled to the fiducial run labelled as Length=1, Mass=1. The circles represent the evolution of the Length=1/6 case using 5 times more particles.

Table 1. Bar parameters

Length	Mass	Real length (a)	$M_b/M_{halo}(a)$
1	1/2	0.067	0.25
1	1	0.067	0.5
1	2	0.067	1.0
1	3	0.067	1.5
1/2	1/3	0.033	1.0
1/3	1/10	0.02	0.5
1/6	1/20	0.01	0.5

the resonance quickly compared to the period of the resonant orbit. As long as the angular momentum is transferred in this *fast* limit (Tremaine & Weinberg 1984, hereafter TW), the torque scales as M_b^2. We saw in Paper I that some resonances and especially ILR have contributions from the *slow* limit, for which the torque scales as $M_b^{1/2}$. Moreover, for strong bars, most of the low-order resonances are in the transition region between these two regimes, rapid slowing not withstanding. The interactions that lead to orbits exchanging angular momentum at resonance are described in Paper I. The total angular momentum of a bar is proportional to its mass:

$$L_z = I_b\Omega_p \propto M_b R_b^2 \Omega_p \tag{13}$$

If we assume that all angular momentum transfer is in the fast limit, then

$$\dot{L}_z \propto M_b^2 \tag{14}$$

and we can compare simulations of different bar mass M_b, bar length a, and bar growth time $A(t)$ as follows. Let the ratio of the bar mass to the halo mass inside of the bar radius be $\mathcal{M} \equiv M_b/M(a)$. If we scale the time by $\mathcal{M}/\Omega_p$ and the angular momentum, L_z, by $L_{z\,init}\mathcal{M}$ then all the evolution histories should be the same. Remember that this is if the fast-limit scaling applies. Alternatively, if we assume that all the angular momentum transfer is in the slow limit, then

$$\dot{L}_z \propto M_b^{1/2}. \tag{15}$$

and We must scale the time by $\mathcal{M}^{-1/2}/\Omega_p$. Finally, we must take into account the bar growth time, $A(t)$. Since the torque mechanism is secular, we expect the degree of evolution to be proportional to the time integral of the applied amplitude, $\tau = \int_0^t dt\, A(t)$ as defined in §4.

Figure 10a shows the evolution of L_z with τ for simulations with different bar lengths and masses, labelled in units of the fiducial model, as outlined in Table 1, and scaled for the fast limit. These simulations also use $N = 10^6$ multimass particles. Bar corotation occurs at a for $t = \tau = 0$ in all of these simulations. The first four cases in the Figure show the scaled pattern speed evolution for the Length=1 bar with a range of masses. In the last three cases we reduce both the bar length and the bar mass. The smallest bar, Length=1/6, is approximately a disk scale length when scaled the Milky Way. With the rescaling
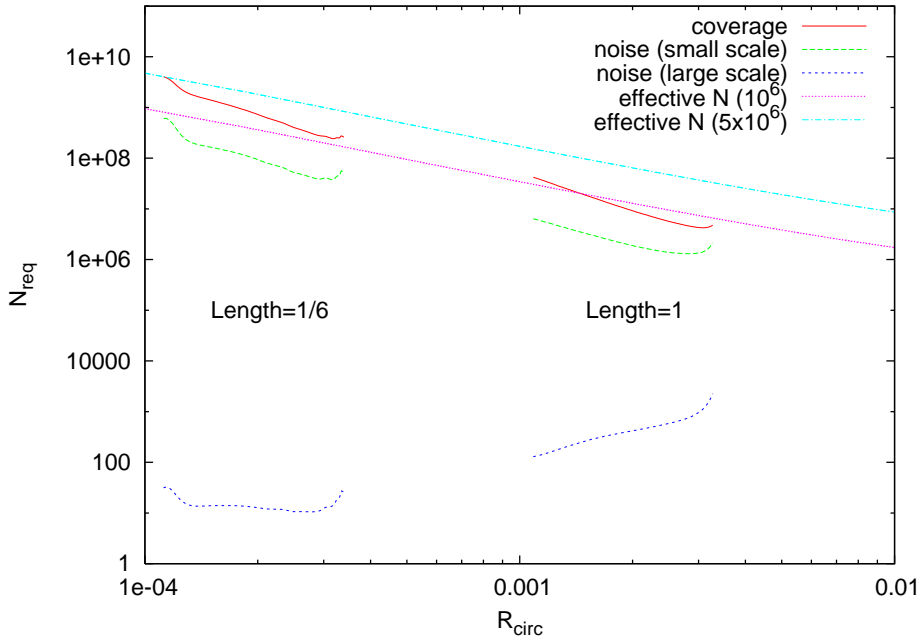
Figure 11. Different particle number criteria from Paper I for a scale-length bar (Length=1/6) and the fiducial bar (Length=1) for the ILR resonance in terms of equal mass particles within the virial radius. Also shown are the effective number of particles for our multimass simulations using 10^6 and 5×10^6 particles.

the evolutions look similar, except for that of the Length=1/6, Mass=1/20 bar, which we discuss more below. The residual differences could be caused either by non-linear interactions, which could cause a breakdown in the linear scaling, numerical artifacts, or contributions by resonances in the slow limit. We make a rough test of the last possibility by taking a equal-part linear combination of the fast-limit and slow limit scalings in Figure 10b. Now all but two of the cases are almost identical; the two discrepant ones are the Length=1/3, Mass=1/10 and Length=1/6, Mass=1/20 bars. Since these two cases are for the least massive bars it seems unlikely that their inappropriate scaling is related to non-linear effects.

Even with these differences, the scaling of $L_z(t)$ is remarkably good over an order of magnitude in unscaled time and, therefore, many of these bars have very different rates of slowing. This may be understood as follows. If we think of performing a periodogram on the bar perturbation, we will see a broadened line in frequency space; the broadening will be inversely proportional the change in $\Delta L_z/L_z$ since the amount of torque lost by the bar controls its instantaneous frequency. The finite time since the formation of the bar also contributes to the broadening. However, the total power, determined by integrating under the broadened line, will be approximately the same since the total rotational kinetic energy is approximately the same. For most resonances, except ILR, the resonance occupies a narrow band in energy. However, for ILR, the energy range may be large. Rapid evolution and subsequent broadening in frequency space can further increase the importance of the ILR contribution (Weinberg 2004, Paper I).

The scaling failure of the small length bars evolutionary histories is most likely caused by numerical deficiencies. In Paper I, we derived three requirements on particle number to model resonant dynamics correctly within N-body simulations. We present these minimum particle number requirements for both the fiducial, Length=1 bar (right-hand side) and the scale-length, Length-1/6 bar (left-hand side) in Figure 11 as a function of radius. Each resonance has different requirements and we show those for the resonance that is most important for both bar slowing and dark matter cusp evolution, the ILR. We only plot the criteria over the range in radii that dominate the ILR for each bar length. Since we plot the number of equal mass particles required within the virial radius, to compare with our multimass simulations, we also plot the equivalent number of equal mass particles in our simulations. Note that in our SCF code, which has no direct two-body interactions, the small scale noise criterion does not apply. Nevertheless, for both bars the coverage criterion is the most stringent. For the small, Length=1/6 bar, one requires about 10^9 particles over the range of radii that dominate the ILR. The same coverage criterion demands only about 10^7 particles for the larger fiducial bar. Comparing this with the effective number of particles in our 10^6 multimass simulations, one can see that the fiducial length bar has a sufficient number of particles to follow the resonant dynamics and the small, Length=1/6 bar simulation does not, as is born out in its poor scaling. To test this idea further, we repeated the Length=1/6 bar simulation using five times more particles, i.e. 5×10^6 multimass particles, which according to Figure 11 should be sufficient. Now the scaled evolutionary history follows that of the other simulations, plotted as the open

(a) Length=1/2

(b) Length=1/3

(c) Length=1/6

(d) Length=1/6, $N = 5 \times 10^6$'
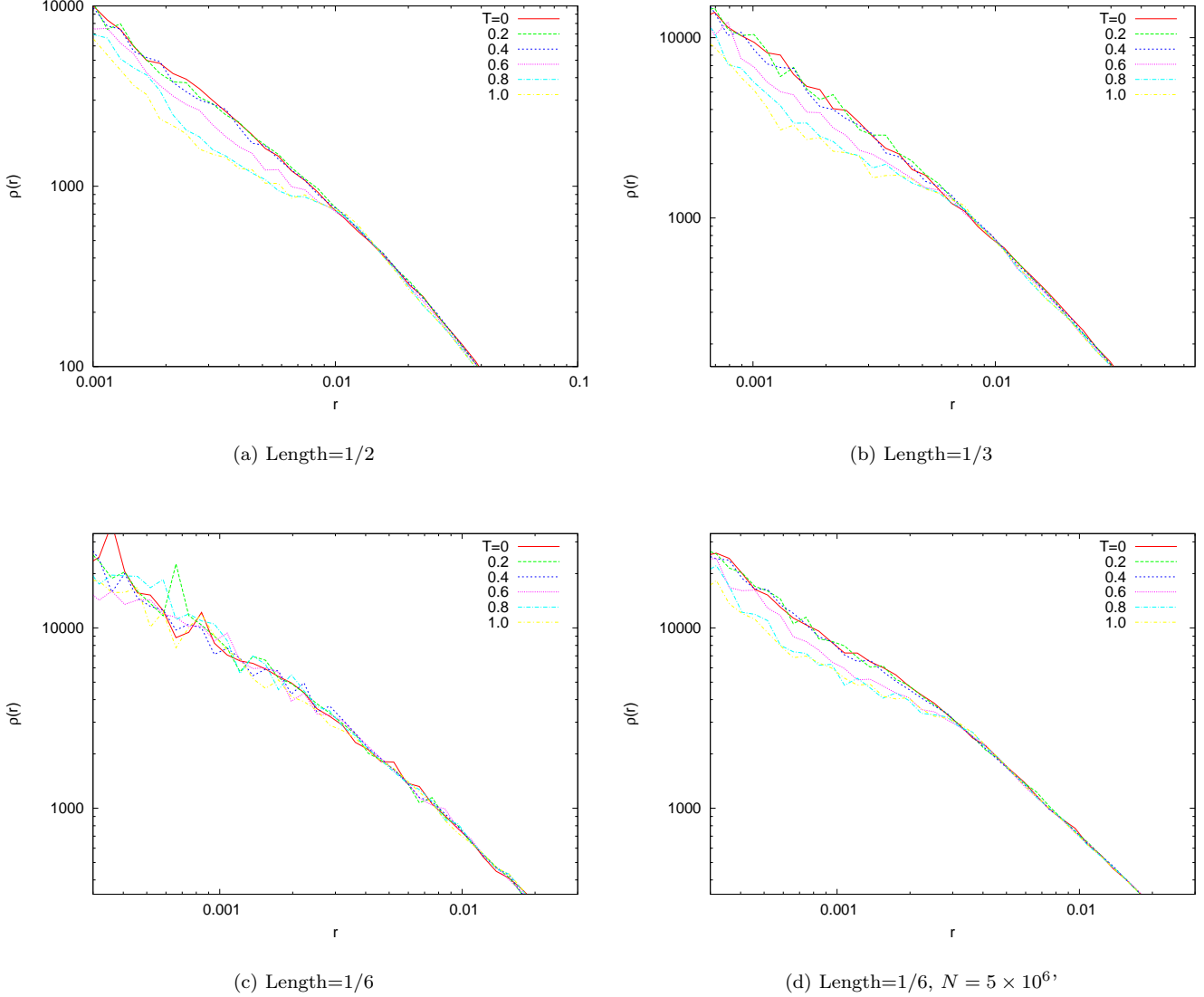
Figure 12. The density profile evolution for three shorter bars. Simulations in the first three panels use $N = 10^6$ multimass particles and the fourth uses $N = 5 \times 10^6$ multimass particles.

circles in Figure 10. This demonstrates the extreme sensitivity of the evolution to numerical deficiencies and the need for a detailed understanding of the dynamics in order to trust the results of N-body simulations.

Like the longer fiducial bar, the shorter bars, except for the Length=1/6 bar, also cause density profile evolution, as shown in Figure 12abc. For the Length=1/2 ($a = 0.033$ or three disk scale lengths) bar and Length=1/3 ($a = 0.02$ or two disk scale lengths) bar one clearly sees the same profile evolution as for the fiducial bar in §4. As predicted by Figure 11, there is no profile evolution in the Length=1/6 ($a = 0.033$ or one disk scale length) bar simulation with 10^6 multimass particles. However, once again if we use 5×10^6 multimass particles, a sufficient number to resolve the ILR resonance responsible for the cusp density evolution according to Figure 11, density profile evolution occurs just as in the three longer bars as shown in Figure 12d. For all four bar lengths the density is reduced within about 30% of the bar radius, independent of bar length if the numerical criteria are satisfied.

In summary, these examples also help clarify several important features of bar evolution in the simulations. For an astronomically realistic bar ending at corotation, a naive estimate places the ILR deep within the cusp. For a scale length bar, the particle number predictions from Paper I suggest that the ILR should not be seen in our simulations with 10^6 multimass particles, and therefore there should be no density profile evolution and indeed there is not. However, for 5×10^6 particles, the effective number of particles near ILR exceeds the coverage criterion and we again see density evolution. Even so, the profiles in the simulations do not evolve at very small radii. It is now clear that these simulations cannot couple to these small radii
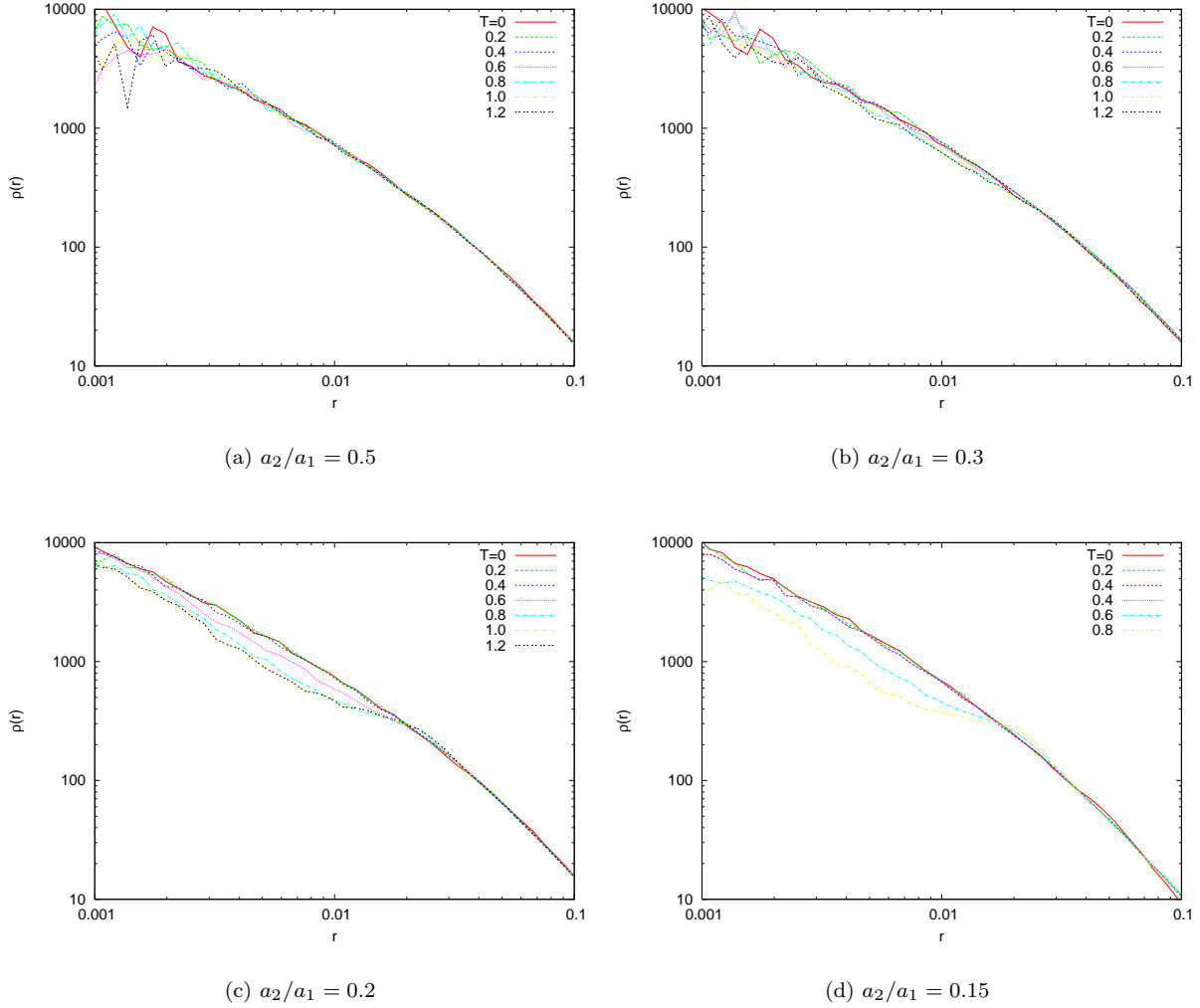
Figure 13. Profile evolution with bars of different axis ratio. Each curve is labelled by time. The initial bar rotation period is 0.3 time units.

solely for computational reasons. Finally, although the multimass initial conditions used here improved the radial resolution and allowed us to recover the correct resonant dynamics using fewer total particles, this technique must be cautiously because it can produce more noise at larger radii.

5.2 Variation in bar shape

Figure 3 clearly shows that a larger major to semi-major axis ratio results in a smaller quadrupole amplitude inside of the bar radius. However, if the quadrupole amplitude becomes too small, there will no way of coupling to the inner halo. We present a series of simulations with $N = 10^6$ (without multimass) with an evolving bar pattern speed to investigate this anticipated trend. The evolution of the halo profiles for different axis ratios is presented in Figure 13. Otherwise, parameters are those from the fiducial run. Each panel shows a different axis ratio a_2/a_1 with fixed a_3/a_1. There is little evolution in the profile for $a_2/a_1 \gtrsim 0.3$ there is no obvious evolution. However, there is clear inner profile evolution for $a_2/a_1 \lesssim 0.2$.

This behaviour is expected from on the criteria described in Paper I (see Fig. 14). The coverage criterion is dominant here as discussed earlier. The sharp threshold is the combined result of increasing amplitude with decreasing axis ratio and more rapid slowing with increasing amplitude. A smaller amplitude perturbation in the vicinity of a resonance yields a smaller resonance width and therefore a higher central particle number requirement. Similarly, a weakly slowing bar will not broaden the ILR to lower frequencies and therefore larger radii where the coverage criterion is also less stringent. These runs suggest that our fiducial simulation is close to the minimum necessary particle numbers. Changing a_2/a_1 from 0.2 to 0.5 makes an order of magnitude decrease in the value of the inner potential. It is, therefore, no surprise that we see critical behaviour as we increase the amplitude of the quadrupole by decreasing the axis ratio a_2/a_1. The description of these trends were presented

(a) small-scale noise

(b) large-scale noise

(c) coverage
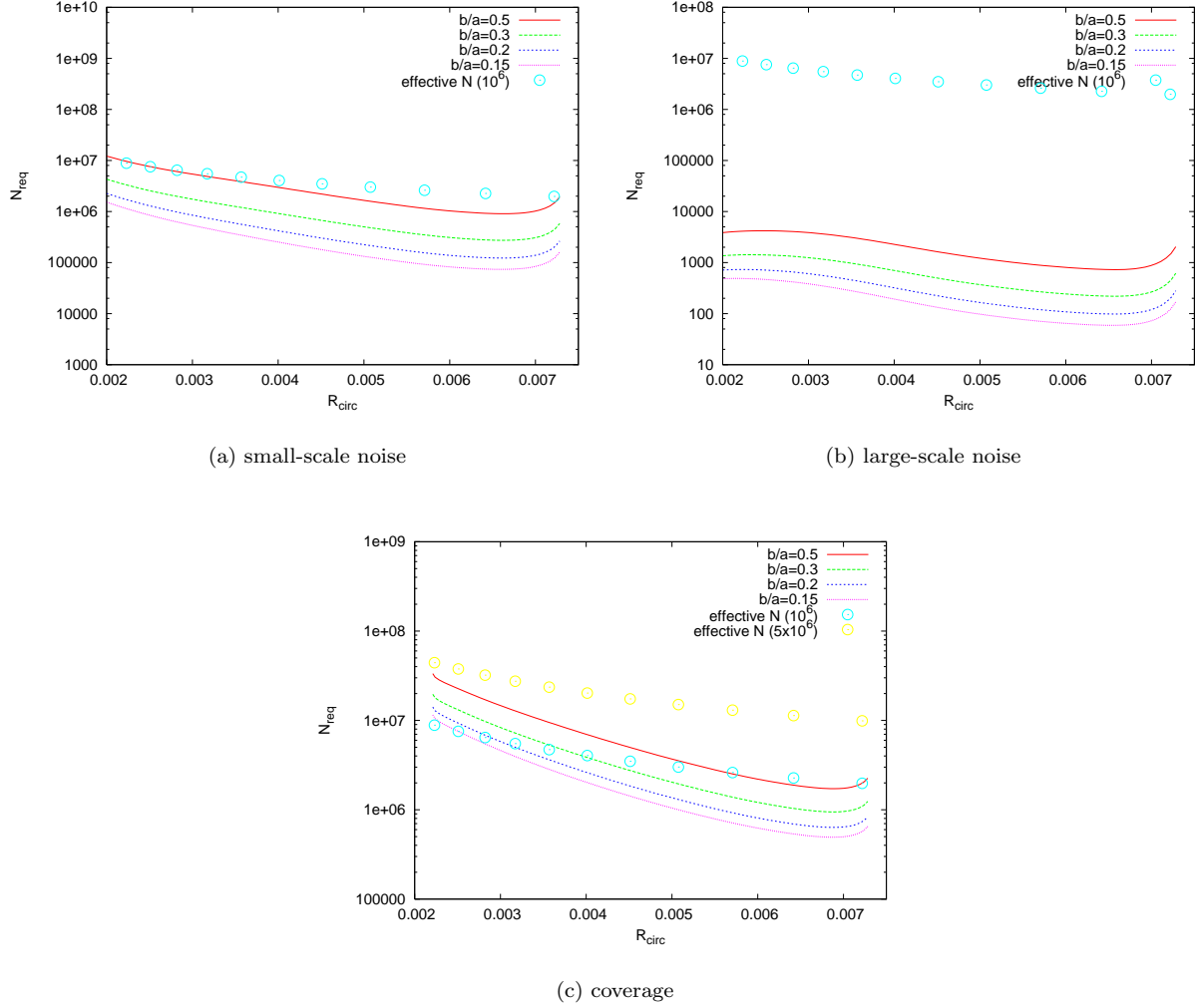
Figure 14. Critical particle number criteria from Paper I for fiducial bar ($a = 0.067$) and but with varying semi-minor to semi-major axis ratios.

in WK. The noise criterion for point particles is also shown in Figure 14. For these cases, the small-scale noise and coverage criteria have similar magnitude. The noise criteria scales as the amplitude of the perturbation potential while the coverage criterion scales as the square root of this value; this explains the difference in range with varying a_2/a_1. The values for the large-scale noise criterion, relevant to our simulation method, are negligible here.

5.3 Variation in halo density profile

The shape of the halo density profile, which determines the existence and location of resonances for a given bar pattern speed, therefore, determines the magnitude and effect of the angular momentum transfer. As an extreme example, we describe the evolution of a bar in a lowered, truncated isothermal sphere (King 1966) with a core radius equal to r_s in the NFW model, using the same total mass as that within the virial radius in the fiducial run. We consider two bar lengths: one with a length of 0.015 (1.5 scale lengths when scaled to the Milky Way) and one the same as the fiducial bar with a length of 0.067 (6.7 scale lengths). The mass of each bar is 50% of the mass of the enclosed dark matter halo mass and initially corotation occurs at the end of the bar. Resonant dynamic theory (see Paper I) tells us that to have a resonance there must be orbits with the right frequency. In addition, within a constant density harmonic core, like in the central regions of a King model, there is no resonance unless $l_1 + l_2 - m = 0$. For the low order resonances, which are most important for the evolution, this is only true for the corotation resonance. However, as the bar slows, the orbits with the right frequency move further out in the halo and the corotation resonance becomes very weak. Therefore, there is no ILR in either case. In addition, for the $a = 0.015$ bar, there are also no (1,0) or (2,-2) resonances, only a small region of OLR, and a weakening corotation resonance. Figure
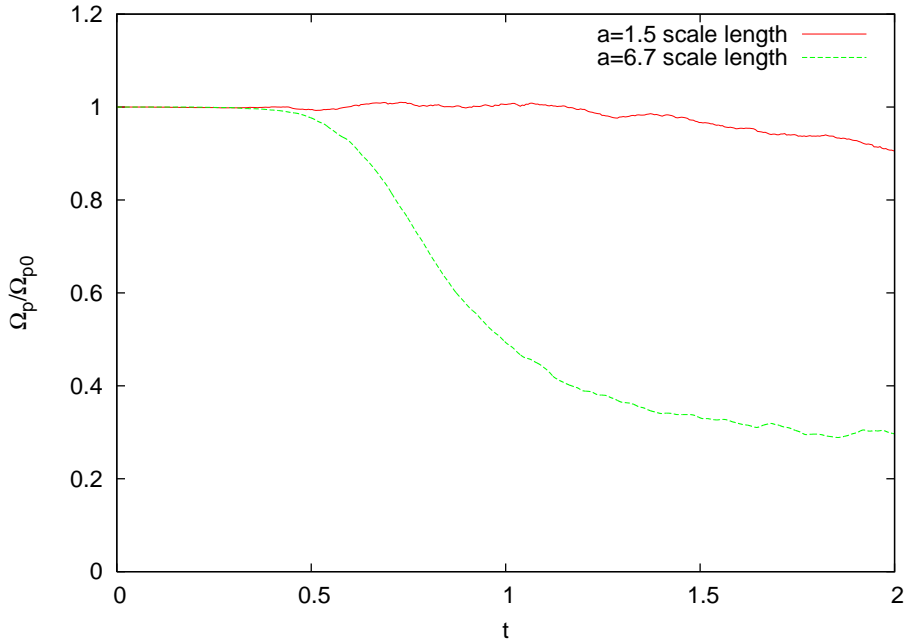
Figure 15. Pattern speed evolution in a King model with $r_c = r_s$ and two different bar models: the fiducial bar with semi major axis $a = 0.067 = r_s$ (6.7 disk scale lengths for the Milky Way) and a small bar with $a = 0.015$ (1.5 disk scale lengths).

15 shows the pattern speed evolution for the two bars. The difference in evolution of the pattern speed, which owes to the different resonances present, is striking.

Next, we compare the evolution of a bar in a King model dark matter halo with the evolution in a NFW dark matter halo. We choose the King Model to have the same mass and a similar concentration as the NFW halo. The bar has a length of 0.01 (one disk scale length when scaled to the Milky Way) and initially corotation occurs at the end of the bar. Figure 16a compares the two initial density profiles. The dark matter density of the King model at one bar length is larger than that of the NFW model and the King density falls below the NFW density at approximate 1/30 of the bar radius. Figure 16b shows the evolution of the bar pattern speed. The bar in the King model does not slow much at all because there is no ILR or DRR, as shown in Figure 16c where we show the position of the resonances in phase space. We have seen (Fig. 5) that these two resonances are responsible for a large fraction of the torque. Although corotation, (2, -2), and OLR are active, their net contributions nearly cancel. Hence, these resonances merely redistribute the angular momentum but do not provide a significant *net* torque on the bar. This is an example of a bar in massive dark matter halo that does not slow, although a significant amount of total angular momentum is exchanged with the halo. Often, people model bar slow down as Chandrasekhar dynamical friction on two point masses, each with one half the bar mass, located at the bar radius (e.g. Sellwood 2004). In this case, such a prescription would have predicted that the King Model bar would slow faster than the NFW. Local Chandrasekhar dynamical friction does not apply to bar slow down, it is the result of resonant dynamics.

We have seen that all aspects of the galaxy model—all the bar and dark matter halo parameters—can affect the subsequent evolution. Therefore, when one compares the differences in evolution between different scenarios, the values that are kept constant determine the outcome. For example, Figure 17a shows the dark matter halo evolution for our fiducial bar in a Hernquist dark matter halo, $\rho \propto r^{-1}(r + a)^{-3}$, with $a = r_s$ and the same mass within the virial radius as our NFW halo. The profile evolution is negligible. However, the mass enclosed within the bar radius is 2.5 times larger than than that in the NFW model. Increasing the mass of the bar by a factor of two, which makes the bar mass 40% of the enclosed halo mass, leads to obvious profile evolution. For comparison, Figure 17c shows the evolution of the same model 17b but without self gravity. The profile evolves only slightly and demonstrates the importance of self gravity in density profile evolution.

As a final example, in Figure 18, we compare the pattern speed and density profile evolution of the fiducial bar in a Hernquist dark halo with that in a NFW halo. However, in this case we match the densities of the inner profile, making the mass inside of R_{vir} no longer the same in the two models. But since the main differences between these halo models occurs at radii well beyond the bar, the bar slow down and density profile evolution haloes is nearly identical.

6 COMPARISON WITH OTHER PUBLISHED WORK

Recent work from different groups have reported a range of conclusions regarding halo induced bar slow down and the subsequent bar-induced halo evolution. As this and Paper I demonstrate, the theory of the dynamical interaction agrees with our simulations, demonstrating its conceptual soundness and applicability. Any differences must either be the result of differences in the simulated bar and halo, which can be in the halo profile, the bar shape, the bar mass, the pattern speed, or the evolutionary history, or to numerical deficiencies. §5 illustrates the diversity of evolutionary results that can result from a range of bar and halo models. We also demonstrated how not satisfying any of the three particle number criteria can result in underestimating bar slow down and the halo density profile evolution. However, if one uses an insufficient number of particles in a simulation, how the evolution proceeds relative to the correct solution will depend on the details of the N-body algorithm. Furthermore, the approach to the correct answer can be sudden, which means that the standard approach of convergence testing can be misleading. Only by fully understanding the underlying dynamics can one fully trust the results of one's N-body simulation.

There are two main differences reported in the literature: the rate of bar slowing and the resulting evolution of the halo profile as a result of the angular momentum deposition. Most groups agree that the bar does slow in most circumstances (HW; Debattista & Sellwood 2000; Sellwood 2006; Athanassoula 2003; McMillan & Dehnen 2005) although Valenzuela & Klypin (2003, hereafter VK) find a more modest slow down. Besides our work (WK; Holley-Bockelmann et al. 2005), no published simulation to date has shown a decrease in the halo central density owing to angular momentum loss from the bar. Of these, Sellwood (2006, hereafter S06) provides sufficiently detailed information so that we can compare directly. S06 describes simulations with an external bar potential similar to those here and in WK. His simulations that use an external bar potential are use two dark matter haloes: a Hernquist model and NFW model. The bar is a fit to an $n = 2$ Ferrers model (Ferrers 1887) also used by HW. S03 makes two main points relevant to our work here: 1) no profile evolution is observed for bisymmetric, even-parity forcing by the bar in either the NFW profile, Hernquist profile or a self-consistently formed N-body bar; and 2) profile evolution is seen if the odd-parity forcing is included owing to a centring artifact. We confirm this latter artifact, attributable to the dipole response, does distort the profile, and addressed this issue in detail (see §3). However, our fiducial run (§4) does not suffer from this artifact and still shows significant halo density evolution. Moreover, we find that even in WK, there is profile evolution before the dipole centring problem dominates the evolution.

There are probably two main reasons for our difference with the bisymmetric (even terms only) runs from S06. First, the Ferrers model fit used in S06 and HW has significantly lower amplitude than the one used here as described in §2.3. Figure 2 shows the fit from HW to Ferrers $n = 2$ model compared with our current model using the same bar mass. The peak of the quadrupole potential differs by a factor of 30. In addition, we have seen that narrower bars have much larger inner quadrupole potentials than rounder bars (see Fig. 3). In particular, S06 and HW use $b/a = 0.5$ while in this paper we use $b/a = 0.2$, which is more typical of a moderate to strong bar. The inner quadrupole for the same homogeneous ellipsoid with these two axis ratios is an additional factor of 10 larger! When we evolve simulations using the parameters in S06 we obtain the same results: no measurable halo evolution. We expect that similar considerations explain the lack of evolution reported in S03 from the self-consistent bar run.

More generally, the dynamics described in Paper I and demonstrated here imply that halo evolution through bar–halo coupling depends on a variety of factors: 1) the underlying halo and disk mass determines the radial location of commensurate frequencies; 2) the bar shape and profile determine the strength of the quadrupole coupling at these resonances; 3) the history of the evolution, e.g. formation and slow down rate, determines the duration of the coupling; and 4) all of the previous three determine the magnitude of the halo evolution. An interesting example of this interplay, suggested by the simulations in S03, is the profile evolution in a Hernquist profile compared to the NFW profile absent the dipole-centring problems. A naively analogous fiducial model puts the bar at the Hernquist model scale length a with the same mass. Surprisingly, the profile evolution for this model is negligible. However, the mass enclosed within the bar radius is 2.5 times larger than that for the NFW profile. Increasing the bar mass by a factor of two gives more comparable enclosed masses and the density profile evolves.

VK attribute the differences between their simulations with other work and analytic estimates to the higher spatial resolution obtainable with their AMT (Kravtsov et al. 1997) Poisson solver. This conclusion is inconsistent at least in part with the dynamics described here and in Paper I. The coupling between the bar and the halo is dominated by the lowest order even multipoles, $l = 2$ in particular, and the contribution for higher multipoles decreases exponentially with l beyond some modest value of l. Although VK use a multimass halo phase space, their effective particle number falls below the coverage and small-scale noise criteria for the ILR, although it is just sufficient for the DRR. The failure of one or more of these criteria may account for some of the discrepancy. Additionally, it is probably worth investigating the numerical noise properties of the AMT algorithm. The simulations of McMillan & Dehnen (2005) also do not have nearly enough particles to satisfy the coverage criterion for ILR, which is the resonance responsible for halo cusp evolution.

The underlying dynamics described by Athanassoula (2003) is consistent with our discussion in Paper I although the emphasis and numerical experiments are quite different so we will not attempt a direct comparison here. However, given the

results with the Hernquist profiles described above and the large scale of her bars relative to the halo scale length, we would expect that the magnitude of the coupling to the inner cusp would be small.

7   DISCUSSION AND SUMMARY

This paper, together with Paper I, has three goals: 1) to explain and clarify the dynamics of resonances in secular evolution; 2) to derive the criteria necessary for a N-body simulation to obtain these resonance dynamics; and 3) to demonstrate the physics of resonances and the applicability of these criteria in N-body simulations. This paper emphasises the bar–halo interaction as a test case for resonant-driven secular evolution but the same techniques can be used generally. We confirm our prediction (Weinberg & Katz 2002, WK) that angular momentum transport can drive substantial cusp evolution within $\approx 30\%$ of the bar radius, mediated by the inner Lindblad resonance. Our N-body simulations corroborate the particle-number predictions of Paper I and illustrate the failure of cusp evolution when the particle criteria are not met. A small number of low-order resonances dominate the angular momentum transport. Therefore, the features and magnitude of the evolution may vary considerably with the model depending on which resonances exist and can couple effectively. More generally, this paper underscores the importance of a prior understanding of the underlying dynamics to ensure a successful simulation.

The importance of resonances is easily motivated. Weak but large-scale perturbations from satellites, self-excited spiral arms, and bars break the axisymmetry of a near-equilibrium galaxy. These perturbations require resonances to redistribute angular momentum which drive the secular evolution. Conversely, without resonances, the torque would vanish and no evolution could ever be driven by these perturbations. For example, the existence of the bar forces an oscillation in the orbits but many of these orbits remain adiabatically invariant to the bar forcing. However, because the bar is slowing or changing at a finite rate, a measurable number of orbits end up with broken invariants and cause a net angular momentum change. However, the change in angular momentum of these orbits varies from positive to negative with initial phase. These larger variations cancel to leave the net positive contribution from the bar. Therefore, a simulation must have sufficient particles to pick up the net effect of this cancellation and sufficiently low noise that an orbit remains coherent over many orbital periods during the resonant interaction.

We have discussed this and several other key points to keep in mind when considering resonant interactions. First, Paper I further elaborates how and why resonances govern the long-term evolution near-equilibrium of slowly evolving galaxies. Without resonances, evolution would depend on astronomical sources of scattering and scattering has an *extremely* long time scale for a quiescent galaxy. Second, resonances are broadened in frequency space by both the finite life time of the bar and the evolution of the bar. Therefore, no bar resonance is ever infinitely thin in frequency space, even one with a constant pattern speed. To first approximation in the ratio of the evolution time scale to the characteristic period, the width of the frequency broadening has no effect on the angular momentum exchange. We demonstrate this empirically in §5.1 using slowing bars of different sizes and masses. This result can motivated by an oscillator analogy. The resonance acts as a forcing whose frequency is changing with time. The rate of change for this forcing corresponds to the resonance sweeping through phase space. An orbit near resonance has the perturbation imposed on the natural orbital motion with a beat frequency. As the orbit approaches the resonance, this beat frequency decreases and the perturbation amplitude increases. The phase of the beat pattern as the beat frequency passes through zero then determines the torque. If the time to pass through the resonance is short, many orbits will be left with a torque from the bar although the change from each will be small. If the time to pass through is long, fewer orbits will receive a net torque but those that do will receive proportionately more angular momentum. In second-order perturbation theory, these two opposing trends precisely cancel and the torque is the same independent of waiting time. In other words, it is the integral under the frequency "line" that matters, not its width. For example, the torque transferred in an idealised perturbation with a constant pattern speed (e.g. Weinberg & Katz 2002) will have the same torque as those with a varying pattern speed over a few dynamical times.

There are two additional conditions necessary for this to work: the angular momentum exchange per orbit must remain linear, $|\Delta J|/J \ll 1$, and the rate of change in pattern speed must be larger than the squared libration frequency for the resonance (the *fast limit* from TW). This simple explanation is complicated by the non-linear dynamics that plays a role when the amplitude of the perturbation is large or the bar evolves slowly. This is the *slow limit* from TW and the resulting perturbation theory is no longer second-order. Paper I shows that this limit is important for the ILR, in particular, and angular momentum exchange in this regime is very susceptible to small-scale noise (see Paper I for details). For strong bars, many of the low-order resonances are close to the transition between these two regimes.

These considerations motivated particle-number criteria for N-body simulations to accurately represent the resonance dynamics. The first, the *coverage* criterion, ensures that phase space density be sufficiently high that the sum of interactions with different phase accurately yields the net torque. The second and third criteria ensures that the gravitational potential fluctuations are sufficiently small that slow-limit resonances can still occur in the simulation. We artificially divide the noise into two regimes: 1) *small-scale* noise refers to fluctuations on interparticle scales or larger. This noise is typical of particle-

particle codes; 2) *large-scale* noise refers to fluctuations on the scale of the inhomogeneity of the galaxy equilibrium. This noise is typical of the basis expansion code used in this study.

Different combinations of these three criteria dominate for different astronomical scenarios and for different codes. We find here and in Paper I that the coverage and small-scale noise criteria dominate. Since our work here uses the basis expansion, our simulations are only affected by the coverage criterion. We show that a scale-length bar (similar to the Milky Way) in an NFW halo with $c = 15$ requires $N \gtrsim 2 \times 10^9$ particles to recover the predicted evolutionary features. We accomplish this large value of N with a multimass phase-space distribution (§2.1) which yields a large effective particle number where it is needed. We strongly encourage others to investigate the importance of these criteria and the noise criteria in particular for their favourite Poisson solver. It is possible, for example, that tree and grid codes might introduce sources of noise not considered here and in Paper I.

The shape and mass of the bar affects these estimates. A bar with the same size and shape as our fiducial model but a smaller mass will have a smaller resonance region and, therefore, require more particles to satisfy the coverage criterion. Paper I shows that this criterion scales approximately as $M_b^{-1/2}$ and our simulations here are in good agreement with this scaling. Similarly, a bar with a 5:1 in-plane axis ratio and shallow or flat surface density (similar to observed strong bars) can provide more than an order of magnitude stronger coupling that a weak oval with a falling surface density. We have illustrated these features with a suite of simulations for bars with differing axis ratios and different particle numbers. We find that the coupling to the inner cusp appears at the bar strength predicted by our particle number criteria.

Resonance-driven secular evolution is related to dynamical friction, which is also a secular process. Traditional Chandrasekhar dynamical friction is non-periodic and works according to the classical scattering explanation. For quasi-periodic systems like galaxies, the correct physical picture is angular momentum transfer near resonances, as described in TW and Paper I at length. Technically, these dynamics can be understood as the superposition of many second-order secular Hamiltonian perturbation theory problems, one for each resonance. In the limit of a small scale perturbation, say a tiny satellite in orbit in a dark matter halo, one can show that these two views give identical results (Weinberg 1986). So dynamical friction operates in quasi-periodic systems because of resonances. This does not imply that one can replace the dynamics described in Paper I with Chandrasekhar's dynamical friction formula. For example, suppose that we removed the band of phase space around some of the low-order resonances in Figure 5 in Paper I and filled it in with unresponsive particles. The torque would vanish but the torque predicted by Chandrasekhar's formula would only drop by a negligible amount. Our numerical experiment of a rotating bar inside of a King-model core (§5.3) shows that the torque is negligible even though the dark-matter density is the same as the rapidly slowing bar in an NFW model, because too few low-order resonances are available to accept torque. A larger bar in the same model may be able to slow through the outer resonances but, without an ILR, the profile evolution would be quite modest. Finally, all halo profiles affect the magnitude and location of the bar–halo torque through the existence of various resonances. For example, by eliminating the ILR and DRR resonances with a small bar-sized core in the dark-matter halo, we can all but eliminate subsequent bar slowing. If, for example, an early bar could flatten an initially cuspy profile, the CDM bar slowing *catastrophe* (Debattista & Sellwood 2000) would be eliminated.

Paper I derives analytically and demonstrates numerically that noise from the finite number of particles leads to fluctuations in the gravitational potential that can change the nature of the resonant interaction that would obtain in the limit $N \to \infty$. In Nature, galaxies have a variety of substructures and the sum total influence of these may be described as *noise*. However, all noise does not have the same spatial and temporal scales as particle noise and, therefore, will have a different impact on the resonances. For example, consider a single satellite orbiting in the halo. We can consider its influence on the galaxy using the perturbation theory described in Paper I and simulations by the methods described in this paper. If we add a few more satellites, the net effect can be treated in the same way as one satellite. As long as the influence of each satellite is coherent over particle orbital times, the same resonant dynamics obtains. As we begin to increase the number of satellites, the combined effect will appear as rapid changes in the force in space and time. As these fluctuations in the correlation length of the gravitational field approach the size of the resonance potential and if the correlation times become smaller than the orbital times, the net effect on the resonances is the same as with small-scale noise. However, if we restrict the population of satellites to large radii, the spatial scales of the fluctuations will be large and the temporal correlations will be long; therefore, this population only weakly effects the dynamics of the inner galaxy. As another example, molecular clouds in a disk, because they are confined to the disk, only contribute noise on scales that are small relative to the dominant halo resonances considered in Paper I. Noise owing to the finite number of simulation particles generates noise at all scales, and because this noise source is generated by the orbits themselves, it naturally couples to the spatial and temporal noise scales in the most effective combination to affect the resonances. In summary, all noise is *not* alike; the spatial and temporal properties of the noise are just as important as its total power. The most obvious sources of astronomical noise—molecular clouds in the disk and substructure in the halo—are not likely to have the same effect as particle noise. The power on various scales for some particular noise source may be computed using the method described in Weinberg (2001).

Finally these stringent particle number requirements does not bode well for *ab initio* galaxy formation simulations (e.g. Steinmetz.Navarro:XX and Governato.etal:05) to correctly capture the correct resonant dynamics. Without doing so, results about disk sizes and rotation curves, some of the most controversial topics, are all suspect. For example, a typical such

simulation that focuses on the formation of one galaxy requires about five times more particles than those required within the virial radius to place the galaxy in its proper cosmological context. Such simulations also use equal mass particles within the virial radius. This means that such a simulation would require at least 10 billion particles to correctly model the disk dynamics! This is just to model the bar-halo interaction. Other processes would likely require even more particles. Such large simulations seem unlikely with our lifetime and hence astronomers will have to invent more clever approaches than pure brute force to make progress in this area of study.

This study motivates the importance of combining simulations with analytic theory to understand galaxy evolution. To recapitulate the introduction, the bar–halo problem was chosen for its overall structural simplicity and, therefore, its amenability to both perturbation theory and N-body simulation. To our surprise, the problem exhibited subtlety at every turn. From perturbation theory, we find that two separate regimes apply: one that scales as the square of the perturbation strength and one that scales as the square root of the perturbation strength. Both regimes apply to problems of astronomical interest. From kinetic theory, we find that these regimes can be affected by relaxation for particle numbers currently used by simulations. We further show that the quantity of torque and the qualitative behaviour of the subsequent evolution depends on most aspects of the model including its history. Because of these subtleties, N-body studies have produced varying results leading to controversy in the literature. Moreover, researchers typically rely on N-body simulation to study astronomical scenarios that appear trickier than this one. For example, the heating of a disk by a satellite may require proper representation of bending modes and subsequent damping through resonant coupling. The range of frequencies and scales in this latter problem is much broader than the bar–halo interaction considered here and, therefore, likely to present similar sorts of surprises that only a combined N-body–perturbation theory comparison will reveal. Additional multiscale problems include the satellite–halo interaction and resonant (pseudo-)bulge formation, and these are likely to require similarly intense levels of dynamical scrutiny.

## REFERENCES

Athanassoula E., 2003, MNRAS, 341, 1179
Binney J., Tremaine S., 1987, Galactic Dynamics. Princeton University Press, Princeton, New Jersey
Brown M. J. W., Papaloizou J. C. B., 1998, MNRAS
Clutton-Brock M., 1972, Astrophys. Space. Sci., 16, 101
Clutton-Brock M., 1973, Astrophys. Space. Sci., 23, 55
Courant R., Hilbert D., 1953, Methods of Mathematical Physics. Vol. 1, Interscience, New York
Debattista V. P., Sellwood J. A., 2000, ApJ, 543, 704
Earn D. J. D., 1996, ApJ, 465, 91
Earn D. J. D., Sellwood J. A., 1995, ApJ, 451, 533
Ferrers N. M., 1887, Quart. J. Pure Appl. Math, 14, 1
Fridman A. M., Polyachenko 1984, Physics of Gravitating Systems II. Springer-Verlag, New York
Hernquist L., Ostriker J. P., 1992, ApJ, 386, 375
Hernquist L., Sigurdsson S., Bryan G. L., 1995, ApJ, 446, 717
Hernquist L., Weinberg M. D., 1992, ApJ, 400, 80
Holley-Bockelmann K., Weinberg M. D., Katz N., 2005, MNRAS
Kalnajs A. J., 1976, ApJ, 205, 751
King I. R., 1966, AJ, 71, 64
Kormendy J., 1982, ApJ, 257, 75
Kravtsov A. V., Klypin A. A., Khokhlov A. M., 1997, ApJS, 111, 73
Lynden-Bell D., Kalnajs A. J., 1972, MNRAS, 157, 1
McMillan P. J., Dehnen W., 2005, ArXiv Astrophysics e-prints
Marletta M., Pryce J. D., 1991, Comp. Phys. Comm., 63, 42
Navarro J. F., Frenk C. S., White S. D. M., 1997, ApJ, 490, 493
Polyachenko V. L., Shukhman I. G., 1981, Sov. Astron., 25, 533
Pruess S., Fulton C. T., 1993, ACM Trans. Math. Software, 63, 42

Pryce J. D., 1993, Numerical Solution of Sturm-Liouville Problems. Oxford

Sellwood J. A., 1981, A&A, 99, 362

Sellwood J. A., 2003, ApJ, 587, 638

Sellwood J. A., 2006, to appear in ApJ

Silverman B. W., 1986, Density Estimation for Statistics and Data Analysis. Chapman and Hall, London

Tremaine S., Weinberg M. D., 1984, ApJ, 282, L5

Valenzuela O., Klypin A., 2003, MNRAS, 345, 406

Weinberg M. D., 1985, MNRAS, 213, 451

Weinberg M. D., 1986, ApJ, 300, 93

Weinberg M. D., 1999, AJ, 117, 629

Weinberg M. D., 2001, MNRAS, 328, 311

Weinberg M. D., 2004, in ASP Conf. Ser. 317: Milky Way Surveys: The Structure and Evolution of our Galaxy Finding the milky way in 2mass. p. 129

Weinberg M. D., Katz N., 2002, ApJ, 580, 627

Weinberg M. D., Katz N., 2005, MNRAS, 000, 000, submitted (Paper I)

(a) Profiles

(b) Pattern speeds

(c) ΔL_z
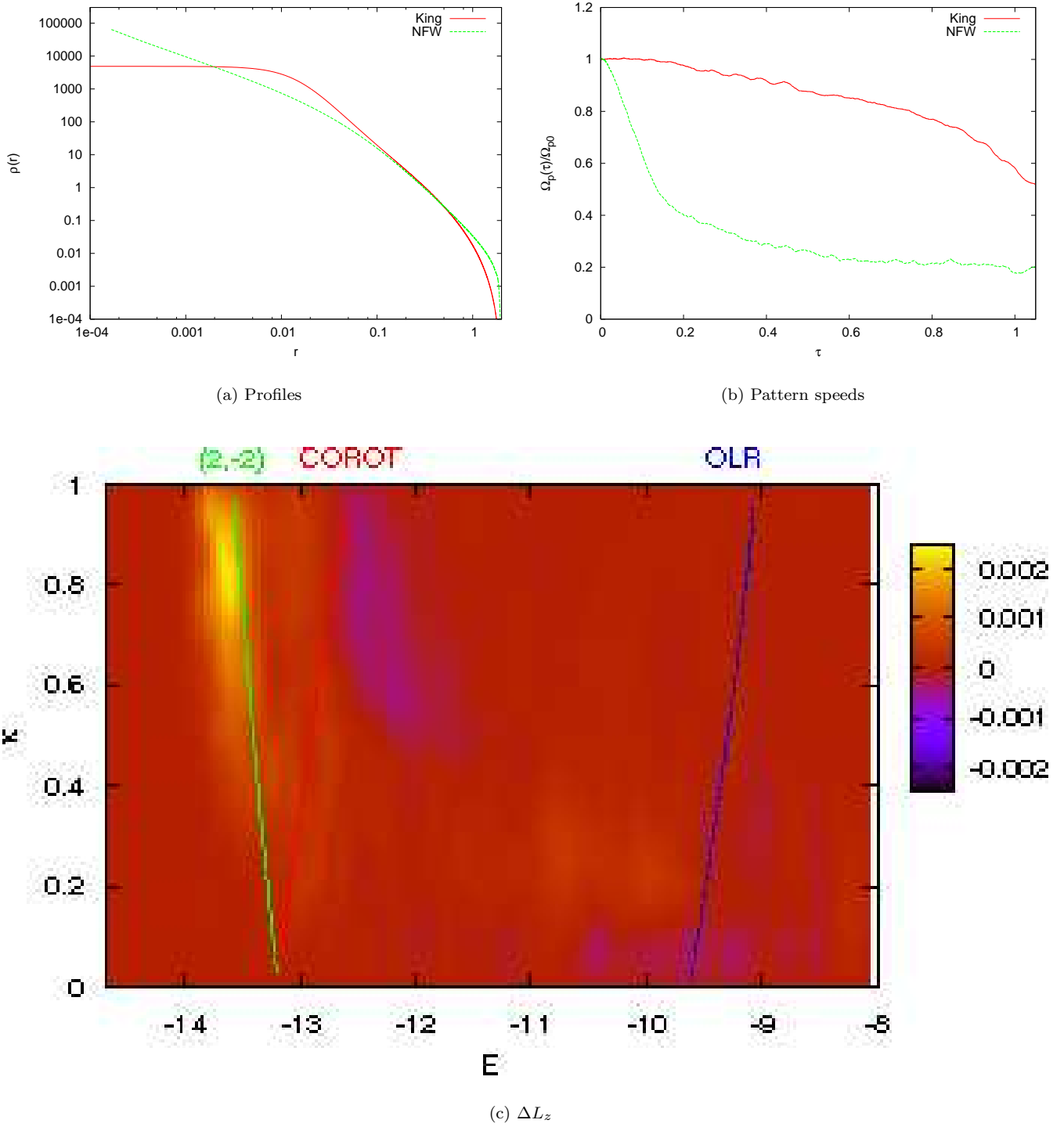
Figure 16. Comparison of bar evolution in a King model dark halo with a NFW dark halo with similar concentrations and the same mass. Panel (a) shows dark-matter density profiles, Panel (b) shows the evolution of the bar pattern speed and Panel (c) shows the distribution of angular momentum change in phase space for the King model. We also overlay the location of the primary resonances as labelled.

(a) Fiducial bar   (b) 2x mass   (c) 2x mass, no self gravity
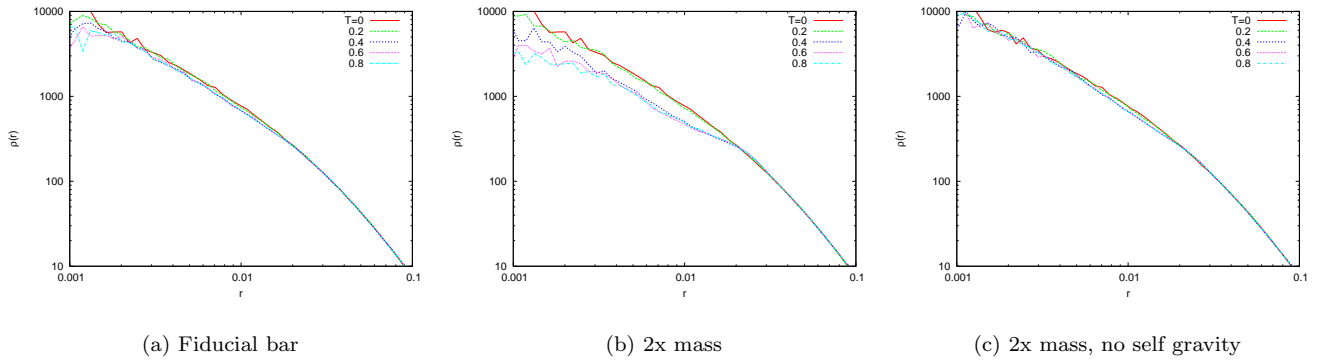
Figure 17. Profile evolution in a Hernquist profile. (a) The fiducial bar from §4 with $a = r_s$. (b) Twice the mass of the fiducial bar. (c) As in (b) but with no self gravity.
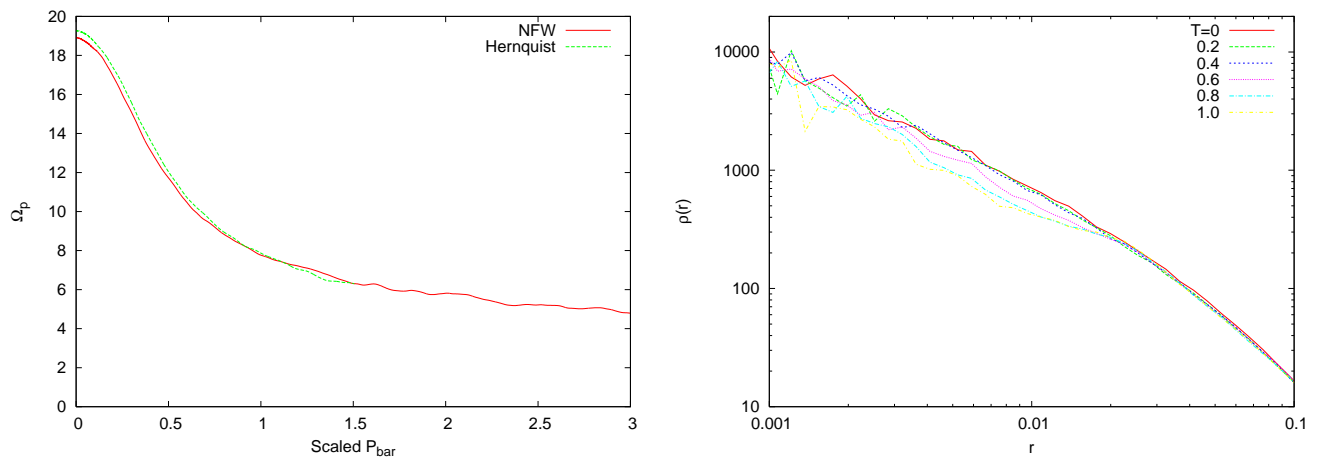
Figure 18. Comparison of evolution in NFW and Hernquist dark haloes with matched cusps. Left: evolution of pattern speed. Right: evolution of profiles in Hernquist halo (compare with Fig. 7).